A Numerical Study of the Local Downslope Wind "Yamaji-kaze" in Japan Part 2: Non-Linear Aspect of the 3-D Flow over a Mountain Range with a Col

By Kazuo Saito

Meteorological Research Institute, 1-1 Nagamine, Tsukuba, Ibaraki 305, Japan
(Manuscript received 25 August 1992, in revised form 12 February 1993)

Abstract

Following the previous work (Saito and Ikawa, 1991a), the three dimensional effect of the orography of the Shikoku Mountains on the *Yamaji-kaze* is studied numerically, focusing on the effect of a col to the flow over a mountain range. The geographical characteristics of the Yamaji-kaze are explained in terms of the non-linear aspect of the three-dimensional flow over a mountain range with a col.

Flow régimes of the three-dimensional flow over a mountain range with a periodic col are examined by use of a linear analytic solution for a homogeneous environmental atmosphere and numerical experiments using a non-hydrostatic model. Two parameters, a non-dimensional mountaintop height lh_m, and the ratio of the amplitude of the col to the mean mountaintop height h_c/h_m, are used to prescribe the mountain shape. The critical values of lh_m which divide the flow regimes are about 20 % smaller in the numerical experiments compared to the linear theory. When the mountain range has a col, wave breaking occurs readily in the lee of the peak of the ridge, and the internal hydraulic jump and reversed flow behind the jump occurs for smaller lh_m compared to the two-dimensional cases. On the other hand, in the lee of the col, a strong wind area easily extends leeward, and the appearance of the jump is unclear in many cases. The behavior of the hydraulic jump is quite sensitive to the existence of the col, while the upstream blocking is rather insensitive to the existence of the col. The response of the hydraulic jump to the existence of a col has qualitative similarities to the behavior of the hydraulic jump in a shallow water flow over a mountain range in a channel of variable width, which has been presented by Saito (1992).

Numerical experiments using the real orography of Shikoku Island and the thermal stratification observed on 21 April 1987 are performed as an example of the simulation of a typical Yamaji-kaze, and the development and movement of the internal hydraulic jump is simulated under a time-changing wind profile. It is shown that the timing of the onset of the Yamaji-kaze, which is too early in the two-dimensional simulation, is ameliorated in the three-dimensional simulation. The geographical characteristics of the Yamaji-kaze can be explained by the reversed flow behind the hydraulic jump which stays in the lee of the Shikoku Mountains and a low-level strong wind area which extends in the lee of the col of the Shikoku Mountains. A further improved surface wind pattern is obtained by inclusion of the surface friction. An improved version of the conceptual model of the Yamaji-kaze is proposed on the basis of the results of the three-dimensional experiments.

1. Introduction

The *Yamaji-kaze* is one of the most well-known local winds in Japan. It is a strong downslope wind which occurs over the northern coastal plain of Shikoku when the lower-level synoptic wind is southerly. It has often caused severe damage and several investigations have been done since olden times. It is accompanied by several characteristic features such as a *Domai* (a northerly wind over Hiuchi-nada, opposite to the southerly downslope wind) and a *Yamaji-kaze front* (a line of discontinuity along which the surface wind direction suddenly changes).

In the previous report (Saito and Ikawa, 1991a; henceforth Part 1), two-dimensional numerical experiments using east-west-averaged orography of Shikoku Island were performed and the following results were presented.

©1993, Meteorological Society of Japan

1) When the non-linearity of the environmental field is strong, an internal hydraulic jump occurs between the wave-induced stagnant layer and the stable layer below it. 2) The surface wind behind the jump becomes weak and a reversed flow develops in the lowest levels in highly non-linear cases. This reversed flow extends its area as time elapses. 3) The location or the moving speed of the hydraulic jump is sensitive to the magnitude of the environmental wind. When the environmental wind is weak, a quasi-steady state in which the jump stays in the lee of the mountains is realized, while when the environmental wind is strong, the jump moves leeward. It seems that this behavior of the internal hydraulic jump conforms qualitatively to that of the hydraulic jump in the shallow water flow shown by the hydraulic theory (Long, 1954; Houghton and Kasahara, 1968). 4) For the orography of the Shikoku Mountains, which have a steep northern slope and gentle southern slope, the hydraulic jump and the reversed flow behind it easily occur. When the orography of the Chugoku Mountains is added, its blocking effect results in a weak effective magnitude of the environmental wind, which allows the reversed flow to occur more readily.

Moreover, 5) development and migration of the hydraulic jump were simulated under the observed thermal stratification and a time-changing wind profile, and 6) a conceptual model of the Yamaji-kaze from its premonitory stage to a mature stage was proposed on the basis of the experimental results.

Although the experiments in Part 1 presented some essential information about the mechanism of the Yamaji-kaze, the simulations were performed under the limitation of two-dimensionality and physical processes such as the surface friction were ignored. A time lag between the onset of the simulated Yamaji-kaze and an observed one remained (Fig. 23 in Part 1). As mentioned later, the Yamaji-kaze is strongly influenced by the three-dimensional effect of the complex real orography.

The first three-dimensional simulation of the Yamaji-kaze was reported by Arakawa and Kimura (1981). They used a hydrostatic model with a horizontal grid distance of 10 km and successfully simulated a strong southerly downslope, but neither a *Domai* nor *Yamaji-kaze front* was obtained. Another report of the three-dimensional experiments of the Yamaji-kaze was given by Saito and Ikawa (1991b). They used a non-hydrostatic model with a horizontal grid distance of 5 km and succeeded in reproducing a southerly downslope in the lee of the col of the Shikoku Mountains as well as a northerly opposite wind over Hiuchi-nada. In their three-dimensional simulation, the opposite wind occurred more readily compared to the two-dimensional simulation of Part 1. Their result suggested that the three-dimensional effect of the Shikoku Mountains influenced the downslope wind and opposite wind over Hiuchi-nada. However, their experiments were preliminary ones with a simple environmental field, and the horizontal resolution was not necessarily sufficient to resolve the hydraulic jump.

As Arakawa (1969) pointed out, strong downslope winds tend to occur in the lee of a col of a mountain range. Although some numerical experiments (*e.g.*, Smolarkiewicz and Rotunno, 1989; 1990; Miranda and James, 1992) have recently studied the mountain flow over a three-dimensional mountain, most of them concern isolated mountains. The behavior of the mountain flow over a mountain range with a col has been seldom investigated, either theoretically or numerically. Most recently, Saito (1992) studied the behavior of a hydraulic jump in shallow water flow over a mountain range in a channel of variable width by expanding Houghton and Kasahara's (1968) theoretical model. According to his results, in the unsteady state in which the jump moves leeward, the moving speed of the jump increases with the decrease of the channel width, and in the quasi-steady state, in which the jump stays over the lee slope of the mountain range, the jump occurs more on the leeward side with the decrease of the channel width. His study suggests that the behavior of the hydraulic jump is strongly influenced by the horizontal divergence or convergence due to the three-dimensionality of the orography.

The purpose of this paper is 1) to study numerically the non-linear aspect of the three-dimensional flow over a mountain range with a col, and 2) to explain the reasons of the locational differences of the climatological features of the Yamaji-kaze. They will be accomplished by use of a three-dimensional non-hydrostatic model with a north-south horizontal resolution of 2 km. In Section 2, the climatological features of the Yamaji-kaze are described, focusing on their locational differences. In Section 3, a description of the numerical model is given. In Section 4, the property of the three-dimensional flow over a mountain range with a col is studied. Linear theory is presented, and the nonlinear aspect of the flow over a mountain range with a col is examined by numerical experiments. The analogy between the hydraulic jump in a continuous atmosphere and in shallow water is discussed. In Section 5, numerical experiments using real orography of Shikoku and observed thermal stratification are performed. The development and movement of the internal hydraulic jump under the time-changing wind profile is simulated. The effect of the surface friction to the Yamaji-kaze is also examined, and an improved version of the conceptual model of the Yamaji-kaze is proposed on the basis of the three-dimensional experimental results. A summary and concluding remarks are given in Section 6.

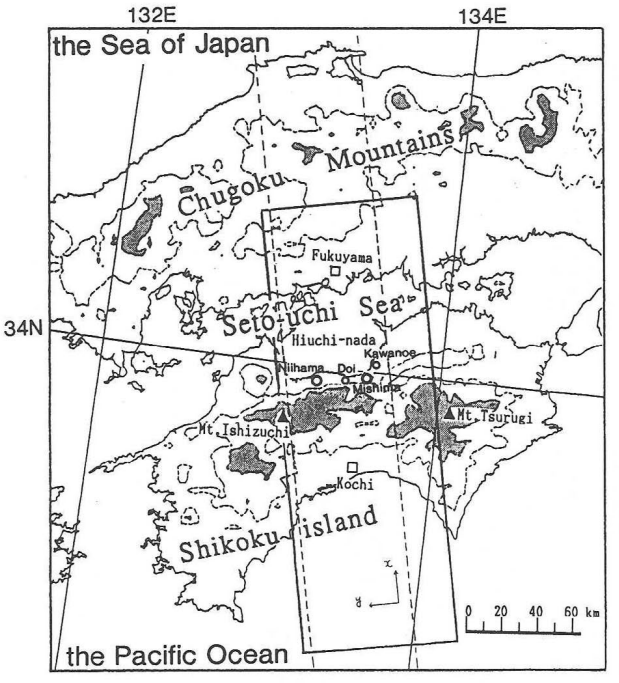


Fig. 1. Geographical map of Shikoku Island, western Japan. The contour interval is 400 m, with the area above 800 m height shaded. Open circles denote the cities (Niihama and Mishima) where automated meteorological stations have been installed, while small open circles denote Doi town and Kawanoe city. Open squares denote the cities (Fukuyama and Kochi) where local meteorological observatories are located. The rectangle framed by a solid line shows the model domain for the 3-dimensional experiments. The broken lines show the area over which the orography is averaged in Part 1.

2. Geographical features of Shikoku and the climatological features of Yamaji-kaze

Figure 1 shows a geographical map of Shikoku, located in western Japan. The island is elongated in the east-to-west direction. In its north central part, the Shikoku Mountains run from east to west. Mt. Ishizuchi (1981 m) and Mt. Tsurugi (1955 m) are located in the western and eastern parts of the Shikoku Mountains, respectively. The height of the Shikoku Mountains gradually decreases from Mt. Ishizuchi to the east, and there is a col in the west vicinity of Mt. Tsurugi. North of Shikoku Island, the relatively flat Chugoku Mountains run from east to west over the central part of the Chugoku Peninsula. Between the Chugoku Peninsula and Shikoku, the Seto-uchi Sea (Inland Sea) lies from east to west. A bird's eye view of the orography of the central part of Shikoku and Seto-uchi Sea framed by a solid rectangle in Fig. 1 is shown in Fig. 4a.

The Yamaji-kaze occurs along the narrow northern coastal plain of Shikoku, from Niihama to Kawanoe, facing Hiuchi-nada (the southern part of the Seto-uchi Sea). The most severe Yamaji-kaze occurs from Doi to Mishima.

The climatological features of the Yamaji-kaze are given in Part 1. Among the remaining features, the following ones can be listed as the most interesting phenomena.

1) A northerly wind, opposite to the southerly synoptic wind is observed as one of the premonitory symptoms (*Sasoi-kaze*). 2) The surface wind direction changes sharply across a line of discontinuity stretching from east to west (*Yamaji-kaze front*). 3) On the north side of the Yamaji-kaze front, a northerly wind opposite to the southerly downslope wind prevails (*Domai*).

Part 1 showed that these phenomena are related to the development and movement of the internal hydraulic jump which occurs in the lee of the Shikoku Mountains.

In Part 1, the orography between the broken lines in Fig. 1 was regarded as the typical orography of the region where the Yamaji-kaze occurs, and two-dimensional simulations were performed using east-west-averaged orography, assuming the two-dimensionality of the Shikoku Mountains. However, the actual Yamaji-kaze does not necessarily occur homogeneously in the coastal plain facing Hiuchi-nada, and the locational differences in the east-to-west direction are in fact not negligible. Figure 2 shows a surface wind analysis of the 27 February 1954 Yamaji-kaze from Niihama to Kawanoe taken from Akiyama (1956). In this figure, northerly winds corresponding to the *Sasoi-kaze* are seen from 09 JST to 13 JST, but these northerly winds are observed only in the western part of the northern coastal plain. Figure 3a shows the time sequences of the surface wind observed at Kawanoe, Mishima and Niihama in the 21 April 1987 Yamaji-kaze. In this figure, the onset of the Yamaji-kaze (the change of the wind direction from northerly to southerly) begins first at Kawanoe, and next occurs at Mishima and Niihama. At Niihama, the western part of the coastal plain, northerly winds are observed intermittently, even during the strongest period of the Yamaji-kaze (from 15 JST to 19 JST). Figure 3b shows the duration of the Yamaji-kaze at Kawanoe, Mishima and Doi observed in 1983. In most events, the Yamaji-kaze begins first at Kawanoe and is followed by Mishima and Doi. Namely, the following locational differences of the geographical features of the Yamaji-kaze can be listed.

1) The strongest wind is observed over the coastal plain around Doi and Mishima. 2) The Yamaji-kaze begins first at the eastern part of the coastal plain, the lee of the col of the Shikoku Mountains. 3) Around Niihama, the western part of the coastal

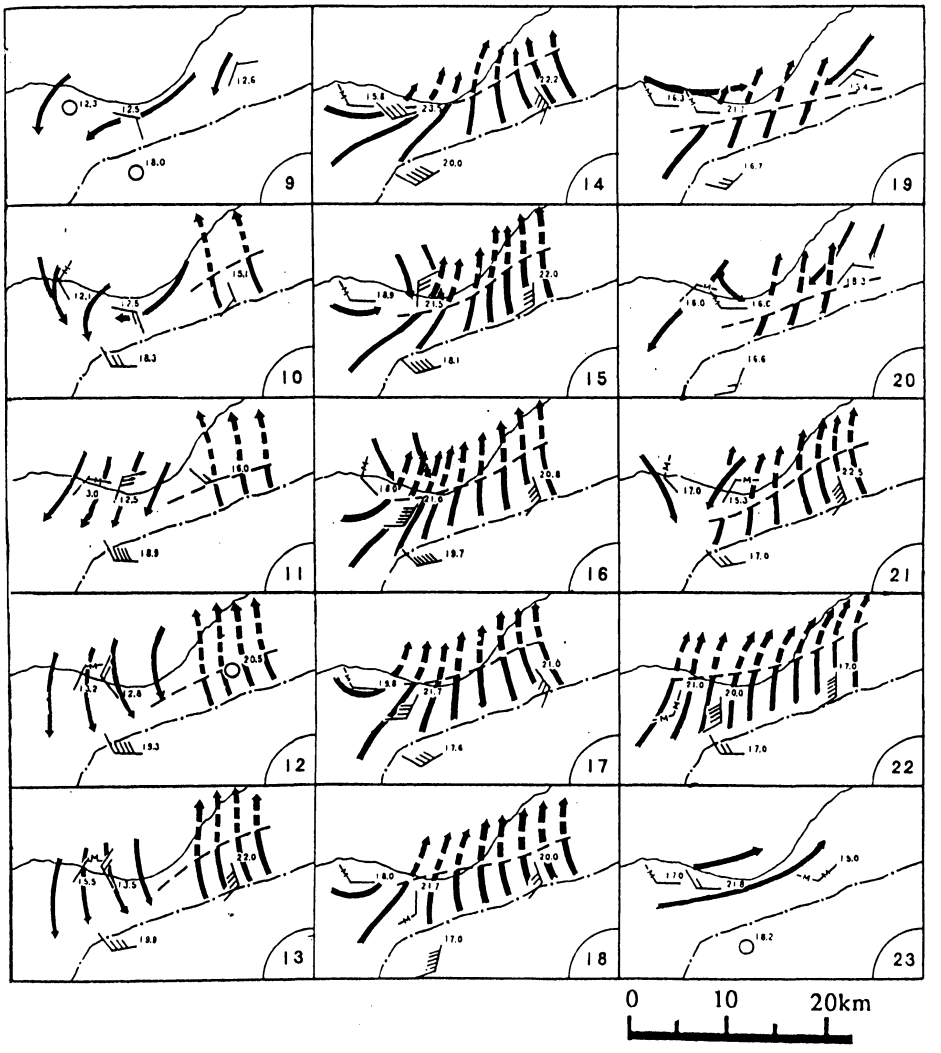


Fig. 2. The analysis of surface winds of the Yamaji-kaze observed from Niihama to Kawanoe on 27 February 1954, adopted from Akiyama (1956). The number at the lower right-hand corner of each section shows the local time (Japan Standard Time, JST). The heavy solid lines show the streamlines on the surface and heavy broken lines show the streamlines separated from the ground. The broken line of each section shows the line where the streamlines detach from the ground surface.

plain, a strong southerly downslope wind is observed, while a northerly wind is also sometimes observed.

The northerly wind around Niihama and the southerly wind around Kawanoe and Mishima are often analyzed as a cyclonic circulation called *Hiuchi-nada depression* (Miki, 1988; *etc.*).

3. Numerical model

The numerical model is a three-dimensional non-hydrostatic model using anelastic equations. The model is the anelastic version of the model developed at the Forecast Research Department of the Meteorological Research Institute (Ikawa and Saito, 1991), and is similar to that used in Part 1 except for the three-dimensional model, unless specifically mentioned.

Following Clark (1977), the terrain-following coordinate,

$$z^* = \frac{H(z - z_s)}{H - z_s}, \tag{1}$$

is used for the vertical coordinate, where z_s is the surface height. The governing momentum and the thermodynamic equations are as follows:

$$\frac{\partial \bar{\rho} G^{\frac{1}{2}} u}{\partial t} + \frac{\partial G^{\frac{1}{2}} p'}{\partial x} + \frac{\partial G^{\frac{1}{2}} G^{13} p'}{\partial z^*} = -\left(\frac{\partial \bar{\rho} G^{\frac{1}{2}} uu}{\partial x} + \frac{\partial \bar{\rho} G^{\frac{1}{2}} vu}{\partial y} + \frac{\partial \bar{\rho} G^{\frac{1}{2}} \omega u}{\partial z^*} \right) - DIF.u, \tag{2}$$

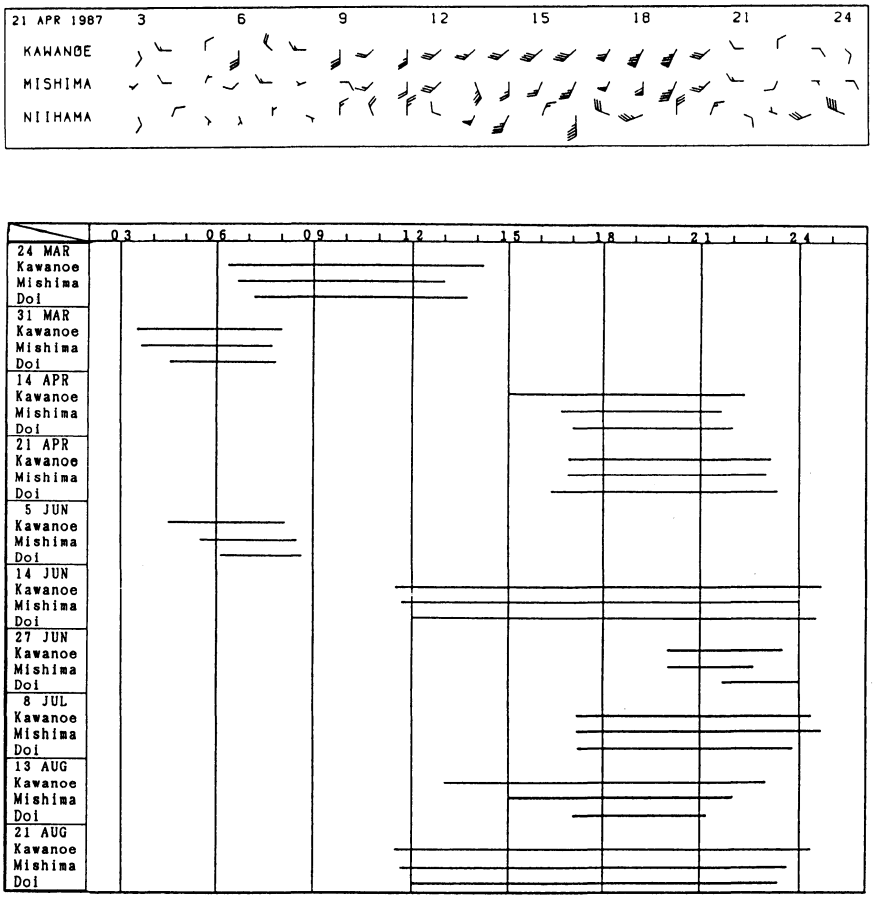


Fig. 3. a) (Upper) Time sequences of the surface wind observed at Kawanoe, Mishima and Niihama on the 21 April 1987 Yamaji-kaze. The numbers in the first row show the local time (JST) (reproduced from Takami and Ohnishi, 1988). b) (Lower) The duration of the Yamaji-kaze at Kawanoe, Mishima and Doi observed since March, 1983 to August, 1983. The numbers in the first row show the local time (JST) (reproduced from Takami, 1990).

$$\frac{\partial \bar{\rho} G^{\frac{1}{2}} v}{\partial t} + \frac{\partial G^{\frac{1}{2}} p'}{\partial y} + \frac{\partial G^{\frac{1}{2}} G^{23} p'}{\partial z^*} = -\left(\frac{\partial \bar{\rho} G^{\frac{1}{2}} uv}{\partial x} + \frac{\partial \bar{\rho} G^{\frac{1}{2}} vv}{\partial y} + \frac{\partial \bar{\rho} G^{\frac{1}{2}} \omega v}{\partial z^*} \right) - DIF.v, \tag{3}$$

$$\frac{\partial \bar{\rho} G^{\frac{1}{2}} w}{\partial t} + \frac{\partial G^{\frac{1}{2}} p'}{G^{\frac{1}{2}} \partial z^*} + g \frac{G^{\frac{1}{2}} p'}{\bar{C}_s^2} = -\left(\frac{\partial \bar{\rho} G^{\frac{1}{2}} uw}{\partial x} + \frac{\partial \bar{\rho} G^{\frac{1}{2}} vw}{\partial y} + \frac{\partial \bar{\rho} G^{\frac{1}{2}} \omega w}{\partial z^*} \right) + \bar{\rho} G^{\frac{1}{2}} g \frac{\theta'}{\bar{\theta}} - DIF.w, \tag{4}$$

and

$$\frac{\partial \theta}{\partial t} = -\left(\frac{\partial \bar{\rho} G^{\frac{1}{2}} u\theta}{\partial x} + \frac{\partial \bar{\rho} G^{\frac{1}{2}} v\theta}{\partial y} + \frac{\partial \bar{\rho} G^{\frac{1}{2}} \omega \theta}{\partial z^*} \right) / \bar{\rho} G^{\frac{1}{2}} - DIF.\theta, \tag{5}$$

where $\bar{C}_s$, $\bar{\rho}$ and $\bar{\theta}$ are respectively the speed of the sound wave, the density and the potential temperature of the reference basic state, dependent only on z. $DIF.$ means diffusion term. The perturbation potential temperature and pressure for the basic state are given by θ', p'. $G^{\frac{1}{2}}$, $G^{\frac{1}{2}} G^{13}$ and $G^{\frac{1}{2}} G^{23}$ are the tensors for the coordinate transformations and ω is the vertical velocity in the z^* coordinate defined as

$$G^{\frac{1}{2}} = 1 - \frac{z_s}{H}, \quad G^{\frac{1}{2}} G^{13} = \left(\frac{z^*}{H} - 1 \right) \frac{\partial z_s}{\partial x},$$

$$G^{\frac{1}{2}} G^{23} = \left(\frac{z^*}{H} - 1 \right) \frac{\partial z_s}{\partial y},$$

$$\omega = \frac{dz^*}{dt} = \frac{1}{G^{\frac{1}{2}}} \left(w + G^{\frac{1}{2}} G^{13} u + G^{\frac{1}{2}} G^{23} v \right).$$

The continuity equation in an anelastic system is given as follows:

$$\frac{\partial \bar{\rho} G^{\frac{1}{2}} u}{\partial x} + \frac{\partial \bar{\rho} G^{\frac{1}{2}} v}{\partial y} + \frac{\partial \bar{\rho} G^{\frac{1}{2}} \omega}{\partial z^*} = 0. \tag{6}$$

The pressure is calculated diagnostically from Eqs. (2), (3), (4) and (6).

To determine the diffusion coefficients, the turbulent closure model is employed. The formulation is based on Klemp and Wilhelmson (1978) and Deardorff (1980), and is similar to that described in Part 1. The mixing length l is calculated according to the local stability N, the sub-grid scale turbulent kinetic energy E and the typical grid scale Δs as follows:

$$l = \begin{cases} \Delta s \text{ ; for unstable case } (N \leq 0) \\ \min\left(\Delta s, 0.76E^{\frac{1}{2}}N^{-1}\right) \\ \quad \text{; for stable case } (N > 0) \end{cases} \tag{7}$$

where

$$N = \sqrt{\frac{g}{\theta}\frac{\partial\theta}{\partial z}}. \tag{8}$$

For Δs, we use

$$\Delta s = \sqrt{\Delta x \Delta z}, \tag{9}$$

instead of the ordinary expression of Δs

$$\Delta s = \sqrt[3]{\Delta x \Delta y \Delta z}, \tag{10}$$

in order to assure the consistency between the two-dimensional simulations and the three-dimensional simulations which are performed in Section 4. As mentioned in Part 1, the development of the hydraulic jump and its associated flow somewhat depends on the formulation of the turbulent closure model, but the differences of the experimental results between the two expressions of Δs Eqs. (9) and (10) are negligibly small for the cases dealt with in this study. In Section 5, an experiment with surface friction is performed. When the surface friction is incorporated, following Mellor and Yamada (1974), the modified mixing length l_f is used to make its value small near the surface as

$$\frac{1}{l_f} = \frac{1}{\kappa(z - z_s)} + \frac{1}{l}, \tag{11}$$

where $\kappa(= 0.4)$ is the Karman constant.

In order to suppress computational noises, fourth-order linear damping, which suppresses mainly 2-grid noises, and a time filter are employed. The time integration is leap-frog, and the time interval is 15 sec.

The upper boundary is a free-slip wall, thermally insulated. In order to prevent a false reflection from the upper boundary, an absorbing layer with Rayleigh friction is imposed in the upper layer, as described in Part 1. The inflow and outflow lateral boundaries (yz-planes) are open where the radiation condition by Orlanski (1976) is employed, while the free-slip wall condition is employed at the side lateral boundaries (xz-planes). The flow obtained by the simulation using these lateral boundary conditions agrees with the flow using a double domain with symmetric orography and periodic side lateral boundaries (see Figs. 5 and 7). Rayleigh damping near the inflow and outflow boundaries, which was employed in Part 1, is not imposed in this study since no significant difference is caused by its inclusion. When the surface friction is incorporated, the surface fluxes are given from a resistance law as described in Ikawa and Saito (1991). Over the sea, the exchange coefficients are determined from the formula by Kondo (1975). Over the land, they are determined from Monin and Obukhov's similarity law for a given roughness length (10 cm) of the ground from the formula by Sommeria (1976). In the simulations in Section 5, only momentum flux is calculated assuming the neutral stratification in the lowest surface boundary layer.

4. 3-D flow over a mountain range with a col

In this section, the property of the three-dimensional flow over a mountain range with a col for the approximation of the Shikoku Mountains is examined. The following simplified orography is used:

$$z_s(x, y) = \frac{h_m - h_c \cos\{2\pi(y - y_c)/b\}}{1 + (x - x_c)^2/a^2}. \tag{12}$$

Here, h_m is the averaged height of the ridge of the mountain range, h_c the amplitude of the col, a half width of the mountain range, b the horizontal interval of the periodic col, and x_c and y_c mean the location of the ridge and the col, respectively. In the case of the Shikoku Mountains, typical values of these parameters are $h_m = 1050$ m, $h_c = 250$ m, $a = 12$ km and $b = 80$ km. Figure 4b shows the bird's eye view of the orography by Eq. (12) represented by 5 km × 2 km grids in which these values of the parameters are used.

4.1 Linear theory of the mountain flow over a mountain range with a col

In this sub-section, the linear theory of the mountain flow over the orography of Eq. (12) is presented in advance of the numerical experiments. The linear analytic solution of the mountain flow over an isolated three-dimensional bell-shaped mountain is calculated by Smith (1980) using a double Fourier transform. In case of the orography of Eq. (12), $z_s(x, y)$ is separable and can be expressed by the Fourier transform in x-direction and Fourier progression in y-direction as

$$z_s(x, y) = \int_{-\infty}^{\infty} Z_k(k) e^{ikx} dk \sum_{n=-\infty}^{\infty} Z_n(n) e^{i2\pi ny/b}, \tag{13}$$

where

$$Z_k(k) = \frac{1}{2\pi}\int_{-\infty}^{\infty} \frac{h_m e^{-ikx}}{1 + (x/a)^2} dx = \frac{a h_m}{2} e^{-a|k|}, \tag{14}$$

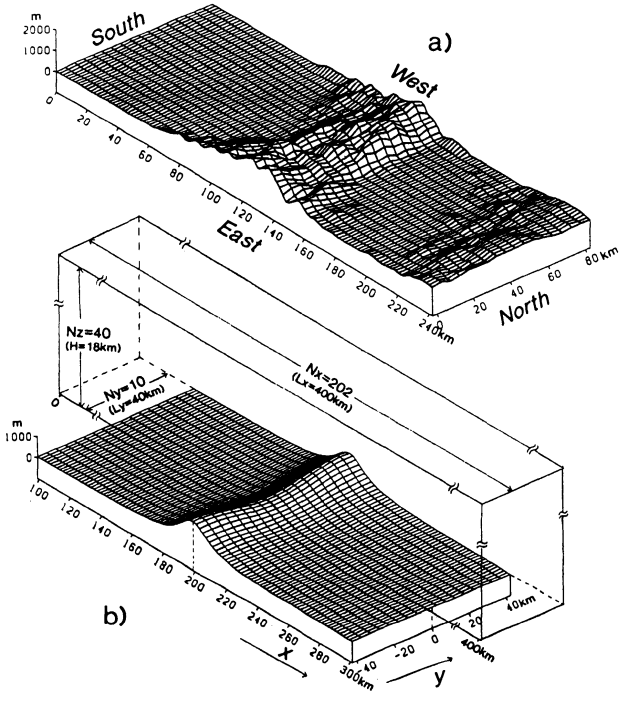


Fig. 4. a) A bird's eye view of the orography of the central part of Shikoku Island framed by the solid line shown in Fig. 1. The grid interval is 5 km × 2 km. b) A bird's eye view of the 3-dimensional bell-shaped mountain with a col expressed by Eq. (12), for the case of $a=12$ km, $b=80$ km, $x_c=199$ km, $y_c=0$ km, $h_m=1050$ m and $h_c=250$ m. The grid interval is 5 km × 2 km.

$$Z_n(n)=\frac{1}{b}\int_0^b\left(1-\frac{h_c}{h_m}\cos\frac{2\pi y}{b}\right)e^{-i2\pi ny/b}dy$$
$$\rightarrow Z_n(0)=1,\quad Z_n(-1)=Z_n(1)=-\frac{1}{2}\frac{h_c}{h_m}. \tag{15}$$

Here, we assumed $x_c=y_c=0$ for simplicity.

For a hydrostatic[1] steady flow of a vertically unbounded stratified Boussinesq fluid over a three-dimensional small-amplitude topography, the following equation for vertical displacement of the streamline $\delta(x,y,z)$ is obtained with environmental wind speed U taken as a constant (Smith, 1980):

$$\frac{\partial^2}{\partial x^2}\left(\frac{\partial^2\delta}{\partial z^2}\right)+\frac{N^2}{U^2}\left(\frac{\partial^2\delta}{\partial x^2}+\frac{\partial^2\delta}{\partial y^2}\right)=0, \tag{16}$$

where N is the Brunt-Vaisala frequency. If $\delta(x,y,z)$ can be expressed by the Fourier transform in the x-direction and Fourier progression in the y-direction, it may be expressed as

$$\delta(x,y,z)=\int_{-\infty}^{\infty}\sum_{n=-\infty}^{\infty}D(k,n,z)e^{ikx}e^{i2\pi ny/b}dk. \tag{17}$$

Substituting (17) to (16), we obtain

$$\frac{\partial^2 D}{\partial z^2}+m^2D=0, \tag{18}$$

where

$$m(k,n)=\frac{N}{U}\frac{\sqrt{k^2+(2\pi n/b)^2}}{k}. \tag{19}$$

With N taken as a constant, and using (14) and (15) as the lower boundary conditions, the following equation for δ is obtained:

$$\delta(x,y,z)=\frac{ah_m}{2}\int_{-\infty}^{\infty}e^{-a|k|}\times\left\{e^{iNz/U}-\frac{h_c}{h_m}e^{im(k,1)z}\cos\frac{2\pi y}{b}\right\}e^{ikx}dk. \tag{20}$$

Once δ is obtained, the vertical velocity component w is easily calculated from the gradient of δ, using the kinematic condition.

Figures 5a and 5b show the vertical cross-sections of w in the xz-planes through the vicinity of the peak and col for the case of $h_m=1050$ m, $h_c=250$ m, $U=8$ m/s and $N=0.01$/s. In this case, the non-dimensional mountain height[2] lh_m $(=Nh_m/U)$ is 0.1, and the normalized amplification of the col h_c/h_m is 0.25. For the calculation of δ, the complex finite Fourier series using array size $NX=400$ is employed due to the complexity of the integration of Eq. (20). As shown in these figures, the patterns of both solutions resemble each other except for the magnitude of the amplitude of the mountain wave.

The perturbation pressure p' can be obtained by use of the hydrostatic relation as

$$p'(x,y,z)=g\int_z^{\infty}\rho'dz'=\rho_0N^2\int_z^{\infty}\delta(x,y,z')dz'$$
$$=\rho_0N^2I(x,y,z) \tag{21}$$

where $I(x,y,z)$ is the vertical integration of δ from an infinite upper boundary where δ becomes 0 to height z. The surface pressure drag, $Drag_{anal}$, is

[1]The nonhydrostatic effect in linear theory is negligibly small in the case dealt with in this study since the product of l $(=N/U)$ and a $(=12$ km) is about 15, which means that the horizontal scale of the mountain is much larger than the distance of a downwind drift during a buoyancy oscillation (see Saito and Ikawa, 1991b).

[2]In Part 1, we called this dimensionless mountaintop height as the *inverse Froude number*. However, this name is not necessarily appropriate as Baines (1987) and Smith (1991) have pointed out, and could be confused with the 'Froude number' in hydraulic theory which is defined as the ratio of fluid velocity to the phase speed of the gravity wave or *internal Froude number* which has been proposed in recent studies (for example, Durran, 1986; Durran and Klemp, 1987; Smith, 1987; Smith and Sun, 1987). In the present study, we call it *non-dimensional mountain height* and describe it as lh_m.

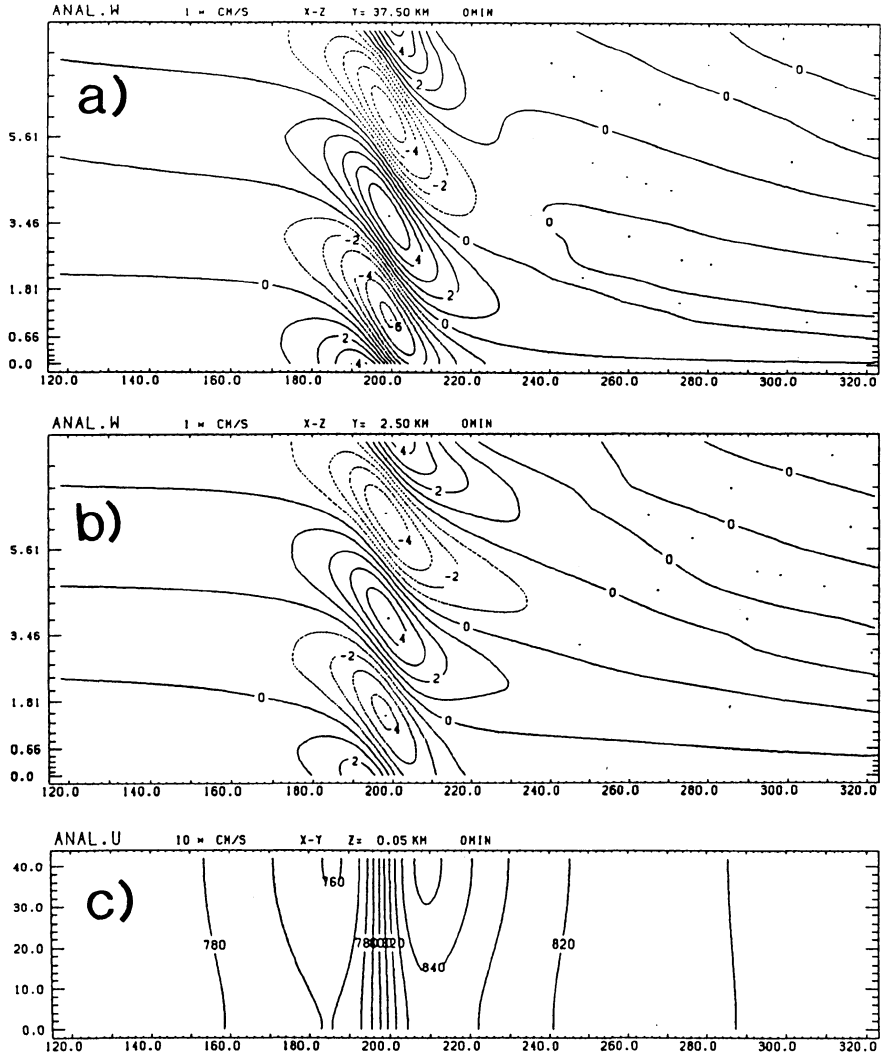


Fig. 5. a) Vertical cross-section of the vertical wind in the xz-plane in the vicinity of the peak of the mountain range obtained by the linear analytic solution ($lh_m=0.1$, $h_c/h_m=0.25$). The ridge is located at $x=199$ km (see Fig. 4b). The contour interval is 1 cm/s. b) As in a) except in the xz-plane through the vicinity of the col. c) Horizontal cross-section of the horizontal wind near the surface ($z^*=50$ m). The contour interval is 10 cm/s. The peak and col of the mountain range are located at $(x, y)=(199$ km, 40 km) and (199 km, 0 km), respectively.

given by

$$Drag_{.anal} = \frac{1}{b}\int_0^b \int_{-\infty}^{\infty} p'(x,y,0)\frac{\partial z_s}{\partial x}dxdy$$
$$= \frac{\rho_0 N^2}{b}\int_0^b \int_{-\infty}^{\infty} I(x,y,0)\frac{\partial z_s}{\partial x}dxdy. \quad (22)$$

Using linearized Bernoulli's law[3]

$$\rho_0 U(u-U) = -p', \quad (23)$$

the horizontal wind u can be obtained as

$$u = U\left(1-\frac{N^2}{U^2}I\right). \quad (24)$$

The magnitude of u decreases with the increase of I and becomes 0 when $I = U/N$. As lh_m increases, u vanishes first at $z = 3/4\lambda$ ($\lambda=2\pi U/N$; vertical wave

[3]Smith (1989a) used non-linear Bernoulli's equation

$$u^2 = \frac{2}{\rho_0}\left(-p' - \frac{1}{2}\rho_0 N^2\delta^2\right) + U^2, \quad (23')$$

and obtained a flow régime diagram in the *lh_m-aspect ratio* plane for a mountain flow over an isolated elliptical mountain (his Fig. 1). As he has admitted, using the linearized Bernoulli's Eq. (23) is more consistent from the standpoint of a linear theory. When Eq. (23′) is used, u becomes 0 at $I=U/2N$, and the critical values of lh_m which divide the flow régimes are factorized by 1/2. Then the wave breaking occurs at $lh_m=0.5$ for a mountain range without a col, which results in a very different value from that predicted by conventional linear theory or numerical experiments for a two-dimensional mountain flow.

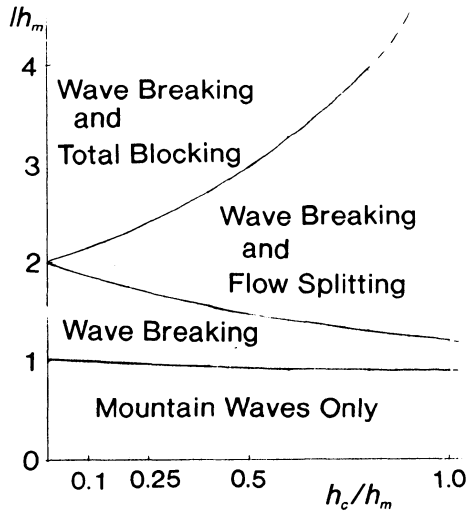


Fig. 6. The flow régime diagram in the lh_m-h_c/h_m plane which is calculated by the analytic solution for the orography expressed by Eq. (12).

length) above the peak of the ridge (wave breaking) and next on the windward slope of the peak of the ridge (stagnant point by the upstream blocking).

Figure 5c shows the horizontal cross-section of u near the surface ($z^*=50$ m) for the same case as in Figs. 5a and 5b. The surface horizontal wind has a maximum on the lee slope of the peak and has a minimum on the windward slope of the peak. With the increase of lh_m, the amplitude of the surface wind anomaly increases linearly, and the minimum point on the windward slope eventually becomes the stagnant point. The pattern is almost symmetric to the ridge, which is located at $x=199$ km.

Figure 6 shows the flow régime diagram in the lh_m-h_c/h_m plane by the analytic solution. In this figure, *Wave Breaking* means the régime in which the wave breaking occurs and *Flow Splitting* means the régime in which an upstream stagnant point develops. The wave breaking occurs at $lh_m=1.0$ for a mountain range without a col, while the critical value of lh_m above which the wave breaking occurs decreases with the increase of h_c/h_m since the mountain wave is enhanced in the lee of the peak of the mountain range. The interesting thing is that when lh_m is large and h_c/h_m is small there is a régime in which u at the lowest level on the entire windward slope becomes negative (*Total Blocking*). In the case of a two-dimensional mountain, *Total Blocking* occurs when $lh_m>2$, but *Flow Splitting* does not occur. In the case of a three-dimensional isolated mountain, *Total Blocking* is never attained.

4.2 Numerical experiments on the mountain flow over a mountain range with a col

In this sub-section, the non-linear aspect of the mountain flow over the orography Eq. (12) in a homogeneous environmental atmosphere is examined by numerical experiments. The model described in Section 3 is used. As mentioned in the former section, the nonhydrostatic effect may not be eminent in the horizontal scale of the Shikoku Mountains with regards to the linear theory. However, the use of the non-hydrostatic model is considered to be more desirable in order to simulate the wave breaking and the hydraulic jump.

The simulation is performed using a half domain of 40 km width, as shown in Fig. 4b, in consideration of the symmetry of the orography with respect to the xz-plane. The horizontal model domain of 400 km $\times$ 40 km is represented by 202×10 grid points with horizontal resolution of 2 km $\times$ 5 km. The peak of the mountain range is located at $(x,y)=(199$ km, 40 km), while the col is located at $(x,y)=(199$ km, 0 km). Typical values of the horizontal scale of the Shikoku Mountains ($a=12$ km, $b=80$ km) are used. Vertically, 40 levels with a variable grid interval of $\Delta z=100$–800 m are employed and the top of the model domain is located at 18 km. The absorbing layer is imposed in the upper layer above the height of 11 km. The Boussinesq approximation is employed.

A homogeneous atmosphere in which a potential temperature lapse rate is 3 K/km is given for the initial condition. In this case, the stability N is about 0.01/s. The numerical experiments are performed by varying lh_m and h_c/h_m. Since the vertical model domain is limited ($H=18$ km), the vertical wave length of the mountain wave, which is estimated at $2\pi U/N$, must be restricted to represent the mountain wave adequately. Consequently, the experiments are performed by varying h_m in the range of 80 m–1050 m with U fixed as 8 m/s for the case of $lh_m<1.3$, and are performed by varying U in the range of 3.5 m/s–8 m/s with h_m fixed as 1050 m for the case of $lh_m>1.3$ (see Table 1). For the initial start-up procedure, the mountain height is initially set at zero and is raised linearly to the ordinary height of the mountain range during the first 320 time steps, which is equivalent to a model time of 80 min. Each simulation is continued until 1920 Δt (480 min).

a) Linear case

Figures 7a and 7b show the vertical cross-section of w in the xz-planes through the vicinity of the peak and col obtained by the numerical experiments at $t=400$ min for the case of $lh_m=0.1$ and $h_c/h_m=0.25$. In this case, both w through the peak and through the col well agree with those by the analytic solution (Figs. 5a, 5b). The pattern of the surface wind (Fig. 7c) is almost symmetric to the ridge at $x=199$ km as in the analytic solution (Fig. 5c), and it is almost steady after $t=80$ min, the mountain has been raised up to the ordinary height.

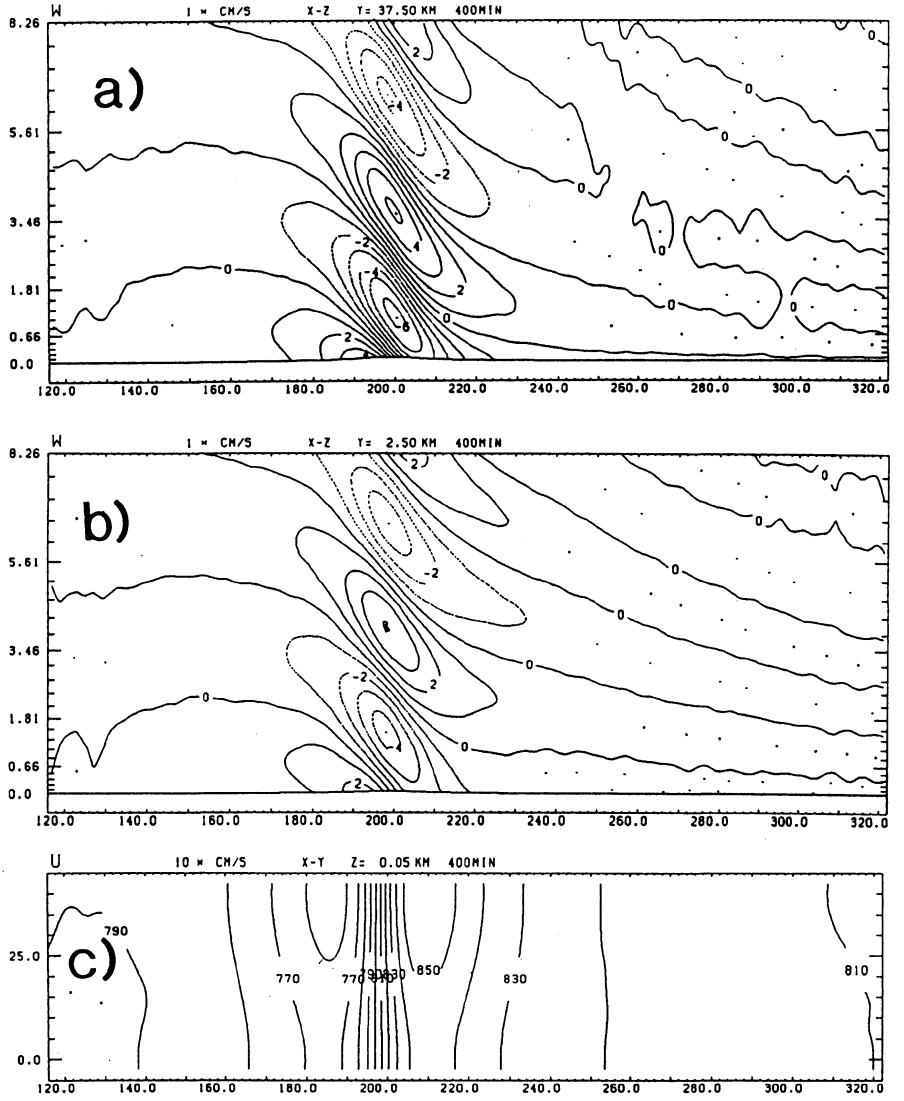


Fig. 7. a)–c) As in Figs. 5a)–c) except by the numerical solution after 400 min.

b) Non-linear case

Figures 8a–8c show the numerical solution by the experiment of $lh_m=1.0$ and $h_c/h_m=0.25$ ($t=400$ min). In this case, wave breaking occurs in the lee of the peak, and a hydraulic-jump-like updraft develops at $x=225$ km (Fig. 8a). On the other hand, in the lee of the col wave breaking does not occur and the vertical velocity in Fig. 8b remains a pattern which is similar to that of the linear case (Fig. 7b). The surface wind is symmetric to the ridge when the mountain has been raised up to h_m, whereas it increases in the lee of the peak with the development of the wave breaking. At $t=400$ min (Fig. 8c), a sudden change of the surface wind speed is seen at the front edge of the strong-wind area. In the lee of the col, a strong wind extends leeward as shown by the 10 m/s contour and discontinuity of u does not develop.

Figures 9a–9c show the results for the case of $lh_m=2.6$ and $h_c/h_m=0.24$, which correspond to a strongly non-linear case ($t=240$ min). In this case, the hydraulic jump in the lee of the peak becomes clear, and a reversed flow develops behind the hydraulic jump as shown in Fig. 9a. On the other hand, in the lee of the col (Fig. 9b), no wave breaking occurs and a discontinuity of u corresponding to the hydraulic jump is not seen. Figure 9c shows the u-component of the surface wind at $t=240$ min. A reverse-wind area develops in the lee of the peak while a strong-wind area in the lee of the col extends leeward. The surface wind on the windward slope of the mountain range becomes negative by the total blocking, and the wind pattern becomes fully asymmetric with respect to the ridge.

In the case of $h_c/h_m=1.0$ (and $lh_m=2.6$), the magnitude of the col is the same as h_m and the peak height is $2h_m$. The orography becomes an (periodic) isolated mountain rather than a mountain

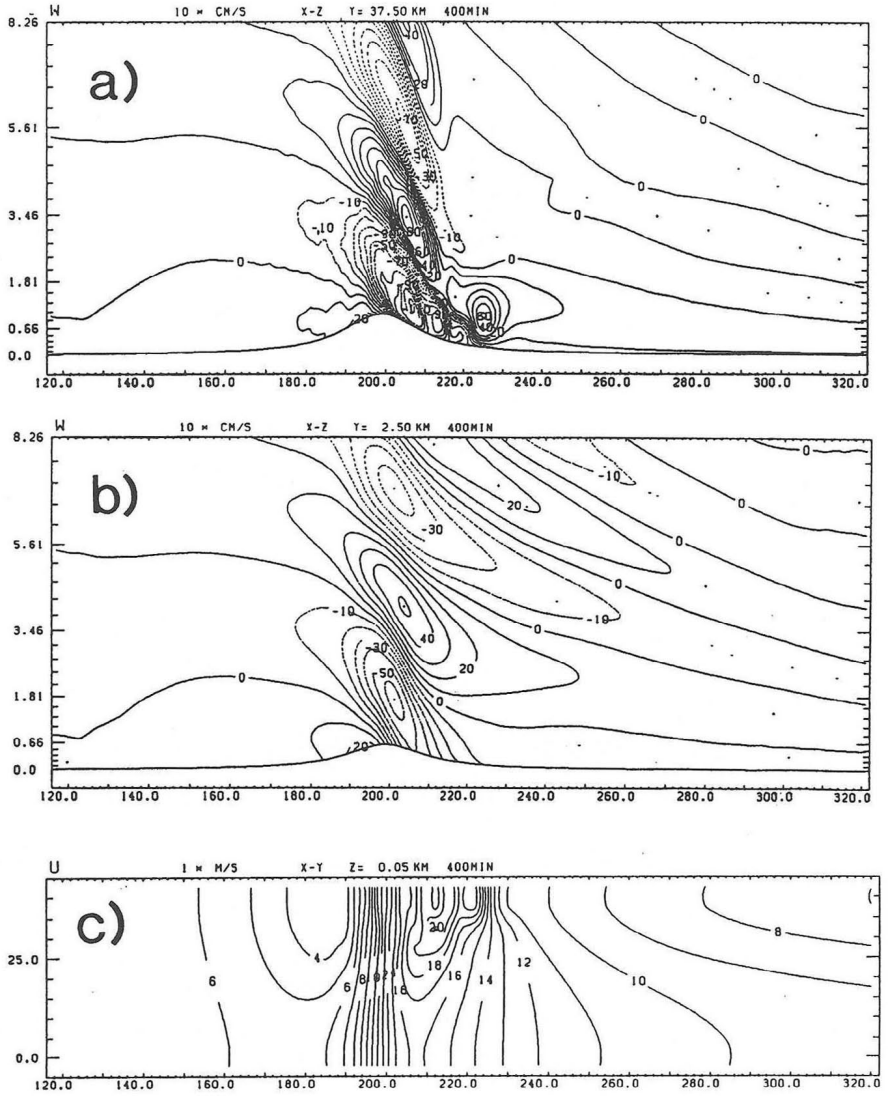


Fig. 8. a)–b) As in Figs. 7a)–b) except for $lh_m=1.0$, $h_c/h_m=0.25$. The contour interval is 10 cm/s. c) As in Fig. 7c) except for $lh_m=1.0$, $h_c/h_m=0.25$. The contour interval is 1 m/s.

ridge. The surface wind flows round the mountain and a reverse flow develops in the lee of the mountain. A cyclonic vortex, which is quite similar to the one of the twin lee vortex reported by Crook *et al.* (1990) and Miranda and James (1992), develops between the reversed flow and the roundabout flow.

The response of the mountain flow to the existence of the col is quite sensitive. Figures 10a–10c show the time sequence of the surface wind for the case of $lh_m=3.0$ and $h_c=50$ m ($h_c/h_m=0.05$). In this case, the jump develops even in the lee of the col due to the strong non-linearity and small h_c/h_m, while the location is very different in the y-direction. In the lee of the peak, the jump is almost stationary at $x=$ 230 km, whereas the jump in the lee of the col moves leeward. In Figs. 10b and 10c, the locations of the hydraulic jump by the two-dimensional simulations in which the ridge heights are 1000 m, 1050 m and 1100 m are shown by Δ, a solid vertical line and ∇, respectively. As shown in these figures, the difference of the location of the hydraulic jump due to the difference of the ridge height in the y-direction by the three-dimensional simulation is much larger than that by the two-dimensional simulation. On the other hand, only a slight difference is seen in the y-direction in the upstream deceleration pattern.

c) Flow régime, surface pressure drag and wind maximum (minimum)

Table 1 summarizes the experimental result for the homogeneous atmosphere. In this table, *W.B.* denotes the wave breaking, *F.S.* the flow splitting, *T.B.* the total blocking, *H.J.* the hydraulic jump, and *R.W.* the reversed wind. The open circles denote the cases in which they appear, and the crosses signify that they do not appear. The triangle means that the appearance of the hydraulic jump is ob-

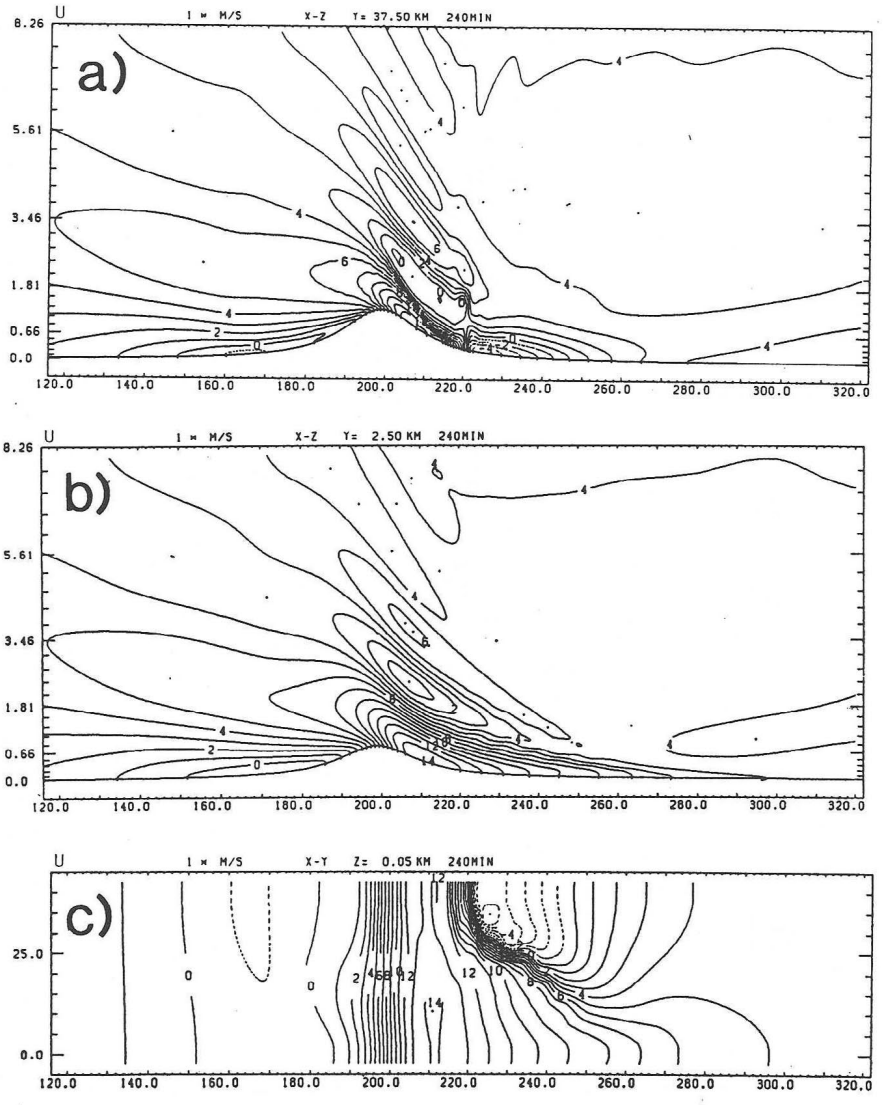


Fig. 9. a)–b) As in Figs. 8a)–b) except for the horizontal wind, $lh_m=2.6$ and $t=240$ min. The contour interval is 1 m/s. c) As in Fig. 8c) except except for $lh_m=2.6$, $t=240$ min.

scure. In this table, $u_{\max}/U$ and $u_{\min}/U$ show the ratio of the maximum and minimum values of the surface wind to U, respectively. The asterisk behind $u_{\min}/U$ denotes the reversed wind behind a hydraulic jump. *N.Drag* is the normalized drag, which is defined as the ratio of the surface pressure drag by the numerical experiment ($Drag_{.num}$) to that by linear analytic solution for two-dimensional bell-shaped mountain without a col ($Drag_{.anal2D}$),

$$N.Drag = \frac{Drag_{num}}{Drag_{.anal2D}} = \frac{\dfrac{1}{40\,\mathrm{km}}\displaystyle\int_{y=0\,\mathrm{km}}^{y=40\,\mathrm{km}}\int_{x=0\,\mathrm{km}}^{x=400\,\mathrm{km}}\left\{p'(x,y,o)\frac{\partial z_s}{\partial x}\right\}dxdy}{\rho_0 U N h_m^2 \pi/4}. \tag{25}$$

These values are averaged values of those from $t=240$ min, after the wave has broken, to $t=480$ min. In the case of $h_c/h_m=0$, the experiments are performed by the two-dimensional model.

Figure 11 indicates the flow régimes in the lh_m-h_c/h_m plane by the numerical solution. Comparing the flow régime shown in Fig. 6, the critical curves of the lh_m which divide the flow régimes are about 20 % smaller than those by the analytic solution. It seems that this difference is caused by the non-linear effect due to the increase of lh_m. In the case of a two-dimensional bell-shaped mountain, it is known that the wave breaking occurs at 0.85 in the non-linear analytic solution (Lilly and Klemp, 1979), which is 15 % smaller than 1.0 by the linear theory.

Figure 12 shows the values of *N.Drag*. In this figure, the heavy solid curve shows the surface pressure drag expected by the linear analytic solution for the three-dimensional mountain range with a col normalized by that for a two-dimensional bell-shaped mountain without a col, that is, defined

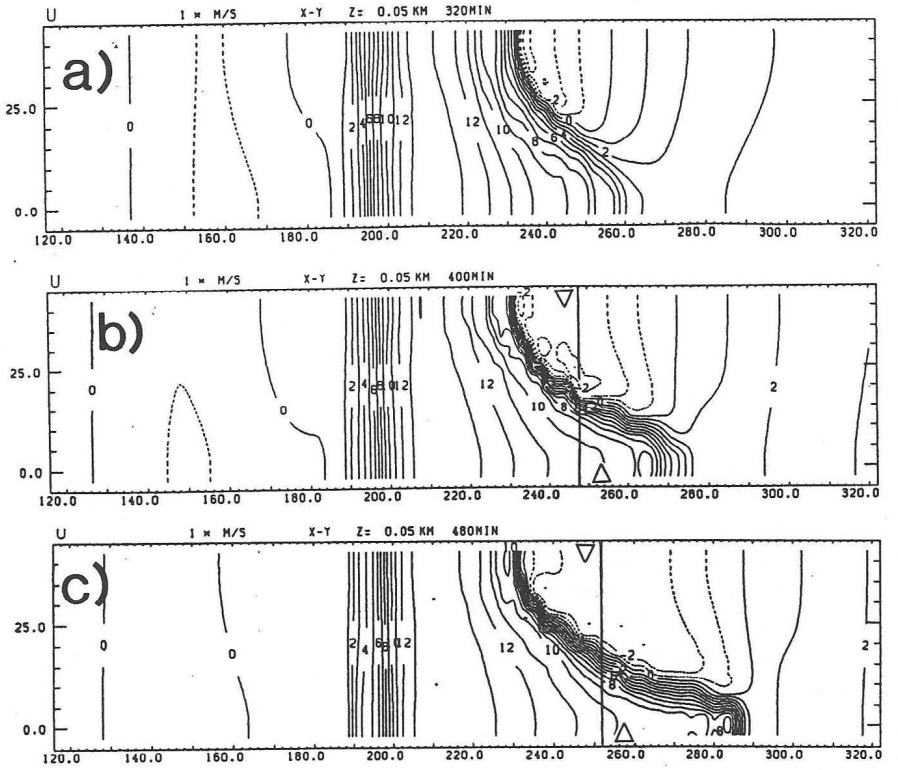


Fig. 10. a) As in Fig. 9c) except for $lh_m=3.0$, $t=320$ min. b) As in a) except at $t=400$ min. The solid line shows the location of the hydraulic jump simulated by the two-dimensional model for $h_m=1050$ m. Δ and ∇ show the locations of the hydraulic jump simulated by the two-dimensional model for $h_m=1000$ m and $h_m=1100$ m, respectively. c) As in b) except at $t=480$ min.

Table 1. Results of experiments for a homogeneous atmosphere.

U	h_m	lh_m	h_c/h_m	*W.B.*	*F.S.*	*T.B.*	*H.J.*	*R.W.*	$u_{\max}/U$	$u_{\min}/U$	*N.Drag*
8	80	0.1	0.	×	—	×	×	×	1.06	0.96	1.01
8	80	0.1	0.25	×	×	×	×	×	1.07	0.95	1.09
8	400	0.5	0.	×	—	×	×	×	1.40	0.77	1.28
8	400	0.5	0.25	×	×	×	×	×	1.46	0.72	1.32
8	400	0.5	0.5	×	×	×	×	×	1.53	0.66	1.44
8	400	0.5	1.0	×	×	×	×	×	1.67	0.50	1.91
8	800	1.0	0.	○	—	×	×	×	2.14	0.62	1.90
8	800	1.0	0.25	○	×	×	△	×	2.53	0.39	2.18
8	800	1.0	0.5	○	×	×	○	×	2.42	0.01	2.29
8	800	1.0	1.0	○	○	×	○	○	2.31	−1.25*	2.29
8	1050	1.3	0.	○	—	×	×	×	3.09	0.36	3.25
8	1050	1.3	0.24	○	○	×	○	×	2.82	−0.02	2.79
8	1050	1.3	0.5	○	○	×	○	○	2.58	−1.30*	2.34
6	1050	1.8	0.	○	—	○	×	×	3.30	0.01	3.28
6	1050	1.8	0.24	○	○	×	○	○	3.30	−1.13*	3.00
6	1050	1.8	0.5	○	○	×	○	○	2.85	−1.48*	2.35
6	1050	1.8	1.0	○	○	×	○	○	3.09	−1.72*	1.93
4	1050	2.6	0.0	○	—	○	○	×	3.73	−0.21	3.03
4	1050	2.6	0.24	○	×	○	○	○	3.88	−1.45*	2.83
4	1050	2.6	0.5	○	○	×	○	○	3.73	−1.84*	2.21
3.5	1050	3.0	0.0	○	—	○	○	○	3.86	−0.34	3.02
3.5	1050	3.0	0.05	○	×	○	○	○	3.91	−0.89*	2.99
3.5	1050	3.0	0.5	○	×	○	○	○	4.02	−1.81*	2.12
3.5	1000	2.9	0.0	○	—	○	○	○	3.79	−0.30	2.99
3.5	1100	3.1	0.0	○	—	○	○	○	3.96	−0.40*	3.04

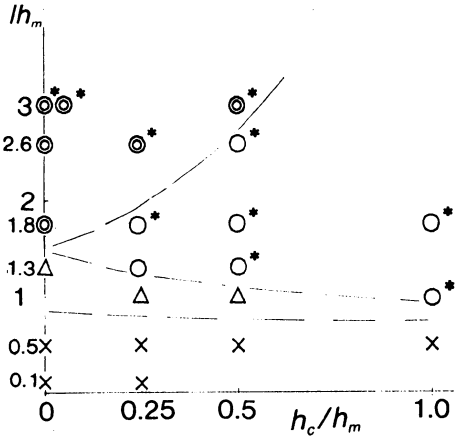


Fig. 11. As in Fig. 6 except by the numerical experiments. Double circles, open circles, triangles and crosses denote total blocking, flow splitting, wave breaking and only mountain waves, respectively. Broken lines show the critical curve of lh_m which divides the flow régime. Asterisks indicate the cases in which reverse winds occur.

by $Drag_{.anal}/Drag_{.anal2D}$. According to the linear analytic solution, the magnitude of the surface drag increases with the increase of the value of h_c/h_m, and at $h_c/h_m=1$ it is about 30% larger than that at $h_c/h_m=0$. In the numerical experiment, the value of *N.Drag* is close to that by the linear theory when $lh_m=0.1$, whereas it is about 30–40% larger when $lh_m=0.5$. In the case where two-dimensionality is good (h_c/h_m is small), *N.Drag* conspicuously increases with the occurrence of the wave breaking and reaches 3.25 when $lh_m=1.3$ and $h_c/h_m=0$. This is the transition to the *high drag state* due to the wave breaking which is reported by Durran (1986). The value of *N.Drag* no longer increases in the region of $lh_m>1.8$, which corresponds to the occurrence of the upstream blocking. It is considered that this is caused by the decrease of the *effective height* of the mountaintop to the mountain flow due to the developing of the low-level stagnant layer by the upstream blocking. In the region $lh_m>1.3$, the value of *N.Drag* rather decreases with the increase of h_c/h_m. Such a decrease of *N.drag* occurs in the region where the flow splitting occurs, and the decrease becomes more conspicuous with the increase of lh_m.

Figure 13 indicates the normalized maximum and minimum values of the surface wind ($u_{\max}/U$ and $u_{\min}/U$). In this figure, *Z*, *Q*, *H* and *F* denote the result by the experiment of $h_c/h_m=0$, 0.25, 0.5 and 1, respectively, and the asterisk means that the minimum wind is the reversed wind behind the hydraulic jump. Solid lines denote the normalized maximum and minimum value of the surface wind by the linear analytic solution for a two-dimensional bell-shaped

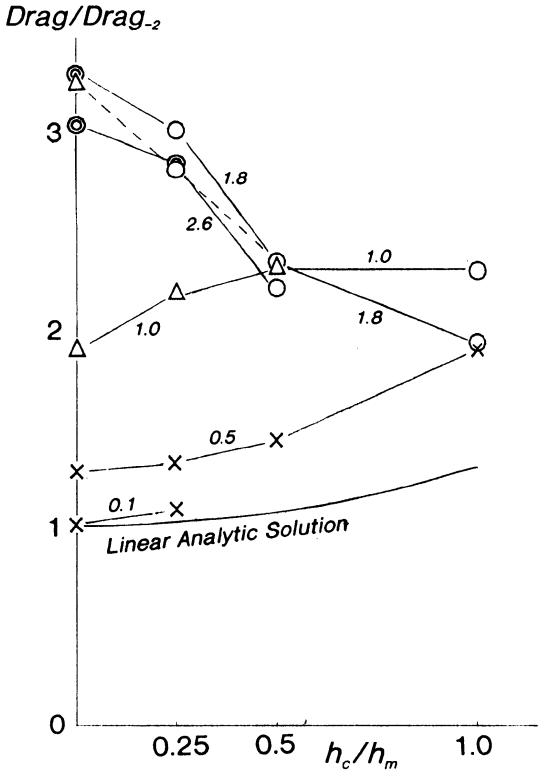


Fig. 12. The h_c/h_m-dependence of the normalized surface pressure drag (*N.Drag*) by the numerical experiments. The meaning of the symbols is the same as in Fig. 11. Numbers show the value of lh_m. The broken line shows the result for the case of $lh_m=1.3$. The heavy solid curve shows the normalized surface pressure drag calculated by the linear analytic solution ($Drag_{.anal}/Drag_{.anal2D}$).

mountain, that is $u_{\max-Z}=1+lh_m/2$ and $u_{\min-Z}=1-lh_m/2$, and broken lines denote those normalized by a linear analytic solution for a mountain range with a col of $h_c/h_m=0.5$ ($u_{\max-H}$ and $u_{\min-H}$) and $h_c/h_m=1$ ($u_{\max-F}$ and $u_{\min-F}$). When lh_m is small enough for no wave breaking, the maximum surface winds are almost equal to or slightly larger than those by the linear theory, and they increase with the increase of h_c/h_m similar to the prediction of the linear theory. With the occurrence of the wave breaking, the maximum surface winds conspicuously increase, but their rate of increase tends to be suppressed with the occurrence of the total blocking or flow splitting. For a two-dimensional mountain, the minimum surface wind occurs on the windward slope and agrees with the predicted value by the linear analytic solution even in the region of a large lh_m. When the mountain range has a col and lh_m is large, the minimum surface wind occurs in the lee of the mountain as the reversed flow behind a hydraulic jump. These reversed flows become evi-

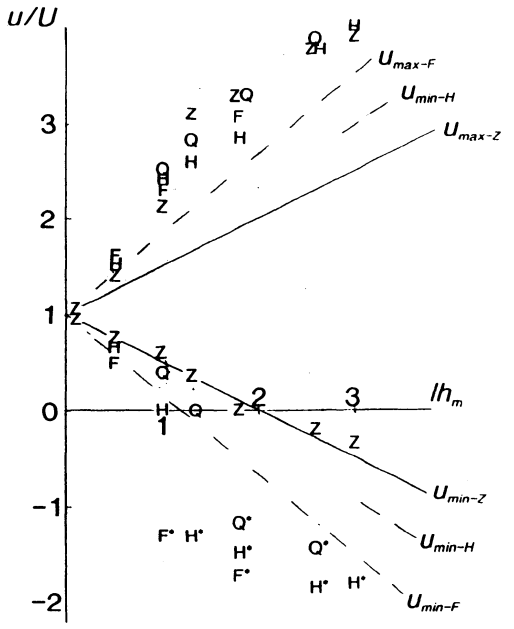


Fig. 13. The lh_m-dependence of the maximum and minimum surface wind. Z, Q, H and F denote the result by the experiment of $h_c/h_m = 0$, 0.25, 0.5 and 1, respectively. Asterisks mean that the minimum wind is the reversed wind behind the hydraulic jump. The solid lines denote the normalized maximum and minimum values of the surface wind by the linear analytic solution for a two-dimensional bell-shaped mountain ($u_{\max -Z} = 1 + lh_m/2$, $u_{\min -Z} = 1 - lh_m/2$). The broken lines denote that normalized by the linear analytic solution for a mountain range with a col of $h_c/h_m = 0.5$ ($u_{\max -H}$ and $u_{\min -H}$) and $h_c/h_m = 1$ ($u_{\max -F}$ and $u_{\min -F}$).

dent in the region of a large h_c/h_m in which flow splitting occurs, and this result is consistent with the numerical experiments for an isolated mountain by Miranda and James (1992). These lee reversed flows cannot be explained by the linear theory and seem to be related to the creation of potential vorticity by wave breaking and/or a hydraulic jump, as suggested by Crook *et al.* (1990) and Smith (1989b; 1991).

4.3 Analogy between the hydraulic jump in a continuous atmosphere and in shallow water

Similarities between the downslope wind in a stratified atmosphere and the flow in shallow water having a hydraulic jump have been known for a long time. According to the hydraulic theory (Long, 1954; Houghton and Kasahara, 1968), the behavior of a shallow fluid over a two-dimensional mountain is categorized by the Froude number and mountain height into four régimes: a sub-critical flow, a quasi-steady flow with a stationary jump, an unsteady flow with a moving jump, and a super-critical flow. The hydraulic jump (downslope wind) occurs when the fluid undergoes a transition from an upstream sub-critical flow to a downstream super-critical flow. The analogy between the atmosphere and hydraulic fluid is clearest in cases where the environmental atmospheric stability has a pre-existing layering, but there is a difference with the vertical transportation of internal gravity waves and the correspondence between the two is not necessarily simple.

Smith (1985) solved Long's (1953) equation for a non-linear steady flow beneath a neutral layer and obtained a critical value of the non-dimensional mountain height where the mountain flow was transformed from a sub-critical flow to a super-critical flow. For the two-layered stratified fluid, several studies have been done to explain its behavior by using Smith's solution and the analogy to the hydraulic fluid (*e.g.*, Durran and Klemp, 1987; Bacmeister and Pierrehumbert, 1988; Ikawa and Nagasawa, 1989; Ikawa, 1990). The fact that, when the wave breaking occurs, nonlinear flow shows hydraulic-like behavior even in the absence of strong structure in the initial stability fields has been pointed out by numerical experiments (Pierrehumbert and Wyman, 1985; Durran, 1986; *etc.*), but their similarities are generally qualitative. Smith's theory suggests that a correspondence can be found between the atmospheric flow beneath a wave-induced stagnant layer and the hydraulic fluid, but it does not yield any information concerning the transient features and the internal hydraulic jump.

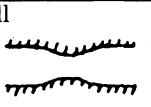
In Part 1, the behavior of the internal hydraulic jump in a homogeneous atmosphere over a two-dimensional mountain without a col was examined, and the analogy to the hydraulic jump in the hydraulic theory was shown. According to the experimental results in Part 1 in which the mountain height and atmospheric stability were fixed, the internal jump remained on the lee slope of the mountain when the fluid velocity was small, while it moved leeward when the fluid velocity was large. In a quasi-steady régime, in which the jump remains stationary, the height of the mountain slope where the jump is located increases with the decrease of the fluid velocity, while in an unsteady régime in which the jump moves leeward, the moving speed increases with the increase of the fluid velocity. The response of the internal jump to the magnitude of the environmental wind speed is analogous to the behavior of the hydraulic jump in shallow water, as shown in Table 2a.

The experimental results in Section 4.2 show that the internal jump tends to stay in the lee of the peak and it does not appear or it moves leeward rapidly in the lee of the col. It is considered that these results are caused by the change of local linearity due

Table 2a. Analogy between a shallow water jump and internal atmosphheric jump over a 2-D mountain.

	strong	←	non-linearity	→	weak
parameter of non-linearity	small	←	fluid velocity	→	large
shallow water fluid (Froud number)	small	←	$U/\sqrt{gd}$	→	large
cntinuous atmosphere	large	←	lh_m	→	small
behavior of lee hydraulic jump	stationary jump: windward side / leeward side	←	moving jump: slow moving / fast moving	→	no jump

Table 2b. Analogy between a shallow water jump and internal atmosphheric jump over a 3-D mountain.

	strong	←	non-linearity	→	weak
effect of 3-D orography	divergence	←	horizontal convergence	→	convergence
shallow water fluid	large 	←	channel width	→	small 
continuous atmosphere	isolated 	←	mountain shape	→	col 
behavior of lee hydraulic jump	stationary jump: windward side / leeward side	←	moving jump: slow moving / fast moving	→	no jump

to the horizontal divergence or convergence by the three-dimensional effect of the orography. Recently Saito (1992) expanded Houghton and Kasahara's (1968) theoretical model and examined the behavior of the hydraulic jump in the shallow water flow over a mountain range in a channel of variable width. According to his results, in the unsteady state in which the jump moves leeward the moving speed of the shallow water jump increases with the decrease of the channel width, and in the quasi-steady state in which the jump stays the shallow jump occurs more on the leeward side with the decrease of the channel width. His study suggests that the behavior of the shallow water jump is also strongly influenced by the horizontal divergence or convergence due to the three-dimensionality of the orography. If we consider the three-dimensional effect of the orography in terms of the horizontal convergence, we can see a similarity between the response of the internal hydraulic jump to the existence of a col and the response of the hydraulic jump in the shallow water flow to the channel width, as summarized in Table 2b.

5. 3-D flow over the Shikoku Mountain in the observed field

5.1 Numerical simulation of the Yamaji-kaze

The actual Yamaji-kaze occurs on the northern slope of the complex real orography of the Shikoku Mountains, and it is likely to be influenced by several factors such as the asymmetry of the Shikoku Mountains, existence of the Chugoku Mountains, surface friction, an inversion layer and a vertical shear of the environmental wind. These factors deform the linear/non-linear aspects of the mountain flow shown in the previous section. For example, the asymmetry of the Shikoku Mountains, which is gentle on the windward side and steep on the lee ward side, tends to enhance the mountain wave, and wave breaking easily occurs, as shown in Part 1. The blocking effect of the Chugoku Mountains allows the reversed wind to occur more readily. In this sub-section, three-dimensional simulations of the Yamaji-kaze are performed using observed thermal stratification and the real orography of the central part of Shikoku including a part of Chugoku Mountains, and it is demonstrated that the experimental results in Section 4.2 are basically applicable to the real situation.

The simulation is performed using the horizontal domain of 240 km × 80 km, which is shown in Fig. 4a. It is represented by 122×18 model grid points with a horizontal resolution of $\Delta x = 2$ km and $\Delta y = 5$ km. Vertically, 32 levels with a variable grid interval of $\Delta z = 40$–1200 m are employed so that the lowest level is located at $z^* = 20$ m. The model top is located at 18 km and the absorbing layer is imposed in the upper layer above the height of 9 km. A Boussinesq approximation is not employed to express the decrease of the density of the reference atmosphere.

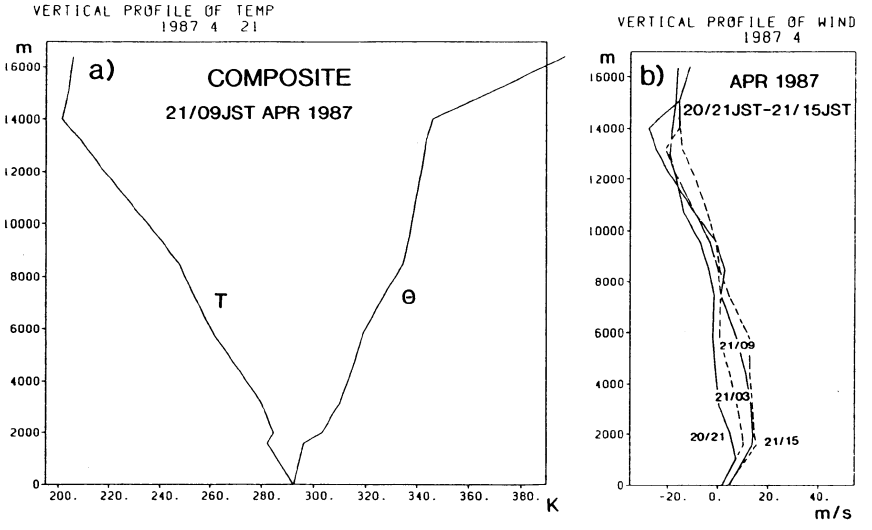


Fig. 14. a) Composite of the vertical profile of temperature (T) and potential temperature (θ) for the soundings at Kagoshima and Shionomisaki at 09 JST 21 April 1987. b) Time evolution of the vertical profile of the composited SSE component of the wind for every 6 hours from 21JST, 20 April to 15 JST, 21 April 1987.

For an initial vertical profile of the thermal stratification of the environmental atmosphere, a vertical profile based on the observation of the Yamaji-kaze on 21 April 1987, which is shown in Fig. 14a, is used. This profile is a composite of the observation of temperatures at Kagoshima and Shionomisaki (for their locations, see Fig. 4 of Part 1), which represents the upstream environment. Figure 14b shows the time evolution of the vertical profile of the SSE component of the averaged wind at Kagoshima and Shionomisaki for every 6 hours from 21 JST, 20 April to 15 JST, 21 April 1987. Considering the gradual increase of the upstream observed wind, the model is started-up initially with no wind on a fixed mountain, and the model environmental wind is gradually increased linearly from zero to the composited profile at 15 JST, 21 April, as shown in Fig. 14b during the 24 hours of the model time. Note that the gradual increase of the environmental wind corresponds to the successive decrease of the non-linearity of the field.

a) The experiment without surface friction

Figures 15a–15c show the time evolution of the x-component (southerly component) of the surface wind ($z^*=20$ m) obtained by a simulation without surface friction. Figure 15a shows the result at $t=$ 8 hrs. At this time, the model environmental wind is 1/3 of the composited wind at 15 JST 21 April. The simulated surface wind increases on the northern slope of the Shikoku Mountains and its maximum is 14 m/s. In the lee of the Shikoku Mountains from Niihama to Mishima (for their locations, see Fig. 1 and Fig. 4a), the area of strong surface wind is restricted by a line of discontinuity which runs from east to west (y-direction in these figures). This line of discontinuity is located just below the hydraulic jump and it corresponds to the *Yamaji-kaze front*. On the north side of the Yamaji-kaze front, the surface wind over the coastal plain is calm or northerly (negative) and corresponds to a *Sasoi-kaze*. A reversed wind, which corresponds to the *Domai*, is seen from Hiuchi-nada to the southern coastal region of the Chugoku Peninsula. On the other hand, in the lee of the col of the Shikoku Mountains around Kawanoe, the area of a strong surface wind extends northward and a break in the Yamaji-kaze front occurs.

At $t=16$ hrs (Fig. 15b), the Yamaji-kaze front shifts further northward and most of the coastal plain of Shikoku is included in the area of the downslope wind. The maximum southerly wind reaches 20 m/s. The break of the Yamaji-kaze front also extends northward and a jet-like area of strong wind is formed in the lee of the col. On the other hand, the wind over the central part of Hiuchi-nada is still northerly, and a cyclonic circulation is formed between this northerly wind and a jet-like strong southerly wind. At $t=24$ hrs (Fig. 15c), the Yamaji-kaze front vanishes and the southerly wind prevails over almost the entire area of Hiuchi-nada. The surface wind is strongest at the northern coast around Doi and reaches 24 m/s.

b) Comparison with the two-dimensional simulation

Figures 16a–16c show the vertical cross-sections of the horizontal wind (u) in the vicinity of Doi (solid lines in Figs. 15a–15c). The strong downslope wind over the northern slope of the Shikoku Mountains extends northward with time. Figures 17a–17c show

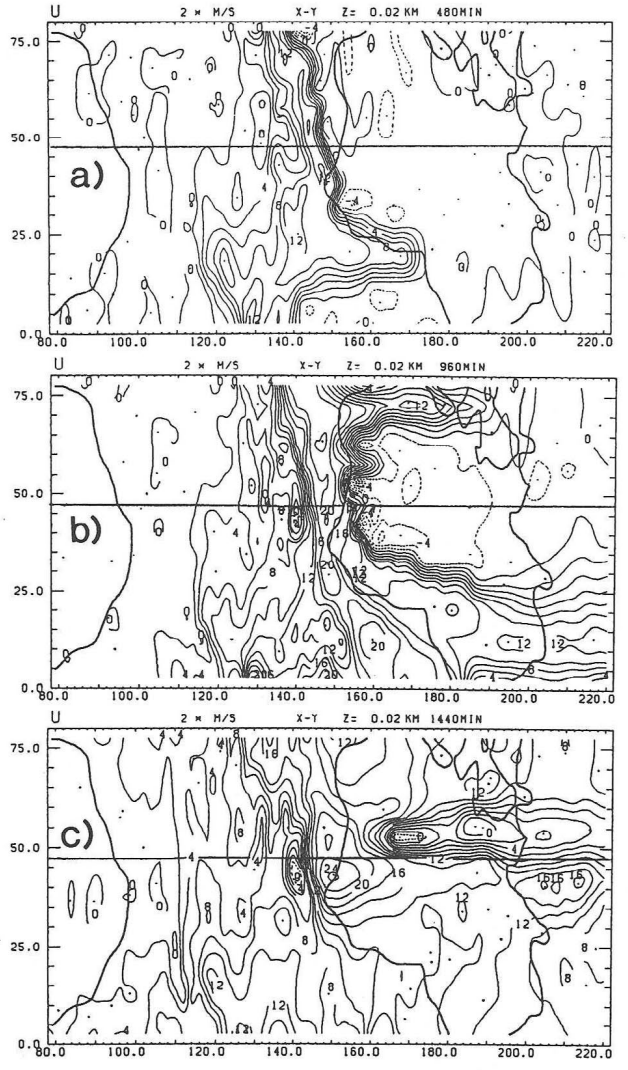


Fig. 15. a) The x-component of the surface wind (u: SSE wind) at $t=8$ hrs from $x=80$ km to $x=220$ km. For the case without surface friction. The contour interval is 1 m/s. The solid lines show the coast line (see Fig. 1 and Fig. 4a). b) As in a) except at $t=16$ hrs. The contour interval is 2 m/s. c) As in b) except at $t=24$ hrs.

the results by two-dimensional simulation in which the averaged orography used in Part 1 is employed. At $t=8$ hrs, the environmental wind is still weak, and the pattern of horizontal wind is not much different between Fig. 16a and Fig. 17a. In both figures, the horizontal wind increases over the northern slope of the Shikoku Mountains, while a weak reversed wind corresponding to Domai is seen near the surface over Hiuchi-nada. The hydraulic jump in Fig. 17a is located at a more leeward position compared to Fig. 16a.

At $t=16$ hrs, in the two-dimensional simulation (Fig. 17b), the hydraulic jump moved leeward rapidly and the northern wind over Hiuchi-nada disappeared. On the other hand, in the three-dimensional simulation (Fig. 16b), the hydraulic jump still remains at $x=155$ km and the northern wind over Hiuchi-nada is also distinct. At $t=24$ hrs, in the two-dimensional simulation (Fig. 17c), the hydraulic jump vanished after it swept out over Hiuchi-nada and the downslope wind over the northern slope of the Shikoku Mountain was rather weakened. The pattern of u shown in Fig. 16c in the three-dimensional simulation is similar to that in Fig. 17b, which corresponds to $t=16$ hrs in the two-dimensional simulation. Namely, the movement of the hydraulic jump is delayed in the three-dimensional simulation.

c) The experiment with surface friction

Figures 18a–18c show the time evolution of the x-component of the surface wind ($z^*=20$ m) for the case with surface friction. At $t=8$ hrs, a break in the Yamaji-kaze front appears in Fig. 15a, but in Fig. 18a the area of strong surface wind is still restricted. At $t=16$ hrs (Fig. 18b), the Yamaji-kaze front breaks around Kawanoe, and the wind around Mishima and Doi begins to increase. Since the model is started up supposing that 15 JST 20 April is $t=0$, Fig. 18c corresponds to 07 JST 21 April, and it is roughly consistent with the onset of the observed Yamaji-kaze at Kawanoe and Mishima (09 JST–10 JST 21 April, see Fig. 3). On the western part of the coastal plain such as at Niihama, the Yamaji-kaze does not begin and the wind is still northerly. This pattern of surface wind seems to be similar to that of the early stage of the Yamaji-kaze shown in Fig. 2. A reversed wind, which corresponds to Domai, is seen over the western part of Hiuchi-nada. The jet-like area of the strong southerly wind shifts westward compared to Fig. 15b, and it may be caused by the difference of roughness between the sea (about 0.2 mm) and the land (10 cm). The cyclonic circulation between this northerly wind and a jet-like strong southerly wind also shifts westward compared to the case without surface friction. These tendencies are consistent with the preliminary report by Saito and Ikawa (1991b) in which the homogeneous environmental wind was used.

At $t=24$ hrs (Fig. 18c) the strong-wind area slightly shifts northward and Mishima and Doi are included in the strong wind area. This strong-wind area is restricted within the northern slope of the Shikoku Mountains where the strong Yamaji-kaze is actually observed. The surface wind is generally weaker than that in Fig. 15c and is about 1/2 of that in the case without friction, but the strongest wind around Doi reaches 20 m/s, which is not very different from that in case without surface friction. The Yamaji-kaze front still remains over the northern coastal plain of Shikoku Mountains and a northerly wind is seen around Niihama. This northerly wind

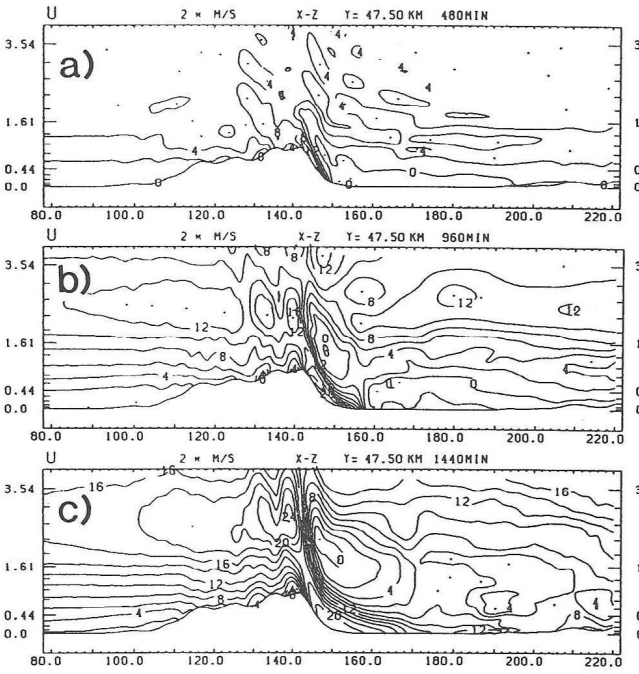


Fig. 16. (left) a) Vertical cross-section of the horizontal wind (u) from $x=80$ km to $x=220$ km through the vertical plane of $y=47.5$ km at $t=8$ hrs for the case without surface friction. The contour interval is 1 m/s. b) As in a) except at $t=16$ hrs. The contour interval is 2 m/s. c) As in b) except at $t=24$ hrs.

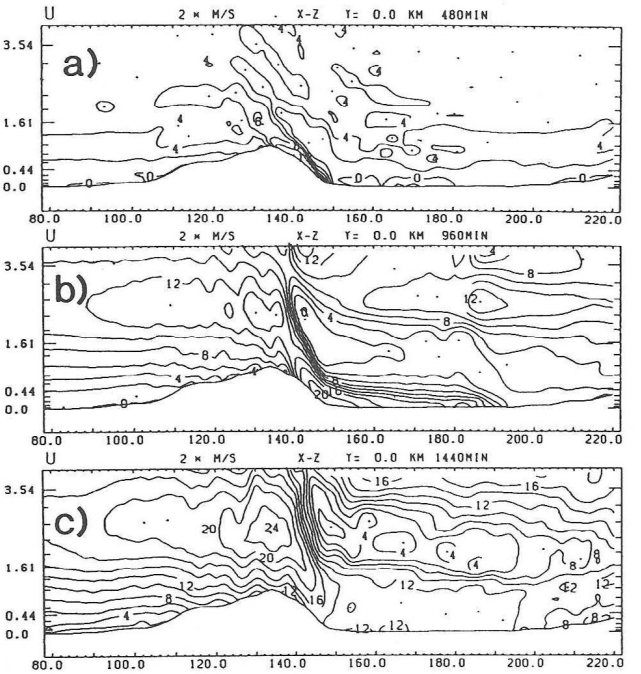


Fig. 17. (right) a)–c) As in Figs. 16a)–c), except by the 2-dimensional model.

seems to correspond to the fact that a northerly wind is often observed around Niihama even during the strongest period of the Yamaji-kaze (Fig. 3a).

Figures 19a–19c shows the vertical cross-sections of the horizontal wind (u), potential temperature (θ) and sub-grid turbulent kinetic energy ($E.T.$) at $t=24$ hrs in the vicinity of Doi (indicated by a solid line in Fig. 18c). The maximum wind over the northern slope of the Shikoku Mountains reaches 20 m/s. The area of a strong downslope wind extends up to $x=154$ km at the level of 100 m above the ground surface, while it is limited by the Yamaji-kaze front to $x=150$ km at the lowest level ($z^*=20$ m) and the pattern is different from that in the case without friction (Fig. 16c). The reversed wind is seen in the lower levels north of the Yamaji-kaze front. The isentropes (Fig. 19b) drop downward in the lee of the Shikoku Mountains and the temperature at the surface increases by about 2 K. This increase of the potential temperature roughly corresponds to the observation at Mishima at this time (Fig. 23 in Part 1). The turbulent energy (Fig. 19c) is large on the surface around $x=150$ km where the Yamaji-kaze front is located, as well as near the mountaintop and hydraulic jump. The large turbulent energy near the Yamaji-kaze front is produced by the strong vertical shear of the horizontal wind and the positive buoyancy due to dropped isentropes. One of the characteristics of the Yamaji-kaze is its very large gust factor (Furukawa, 1966; Takami and Ohnishi, 1988). It can be explained by the large turbulent energy around the Yamaji-kaze front and the existence of the strong wind area just above the surface.

5.2 Conceptual model of the Yamaji-kaze

In Part 1, a conceptual model of the Yamaji-kaze was proposed on the basis of the two-dimensional experiments. It explained the Yamaji-kaze and its associated phenomena by the evolution and migration of the internal hydraulic jump and its associated flows. Although the three-dimensional simulation given in Sections 4.2 and 5.1 basically support this conceptual model, it is also shown that the behavior of the internal hydraulic jump is quite sensitive to the existence of the col of the mountains. An improved version of the conceptual model of the Yamaji-kaze can be proposed considering the results of the three-dimensional experiments given in the former sections.

Figure 20a shows a schematic representation of a conceptual model of the Yamaji-kaze in its early stage. When the southerly synoptic wind is still weak, the hydraulic jump occurs on the lee slope of the Shikoku Mountains. A reversed flow develops just behind the hydraulic jump and a northerly wind is observed over the northern coastal plain of Shikoku Island from Niihama to Mishima. This opposite wind corresponds to the *Sasoi-kaze* which is one of the premonitory symptoms of the Yamaji-

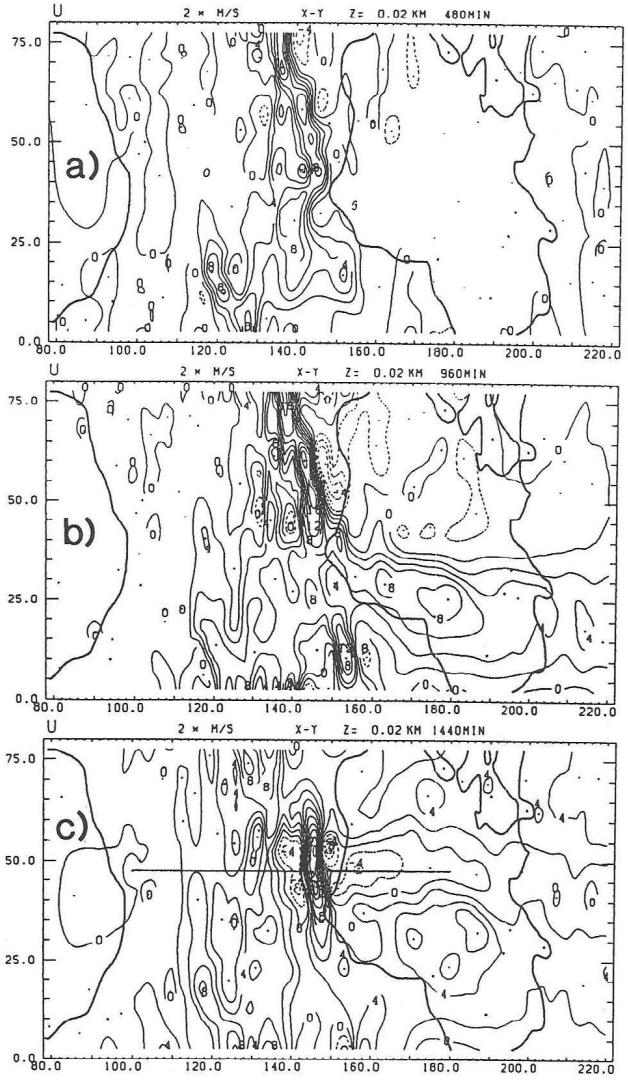


Fig. 18. a)–c) As in Figs. 15a)–c), except by the simulation with surface friction.

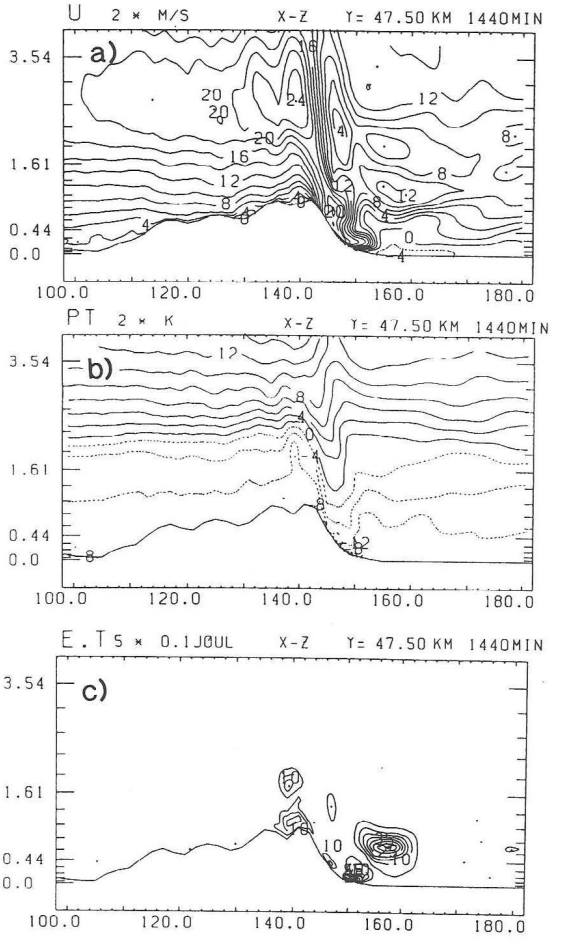


Fig. 19. a) As in Fig. 16c) except from $x=100$ km to $x=180$ km by the simulation with surface friction. The contour interval is 2 m/s. b) As in a) except for potential temperature (deviation to 300 K). The contour interval is 2 K. c) As in a) except for subgrid scale turbulent energy. The contour interval is 0.5 J/Kg.

kaze. At this time, the surface wind near the top of the Shikoku Mountains has already strengthened, and the *Yama-nari*, rumbling over the mountain, can be detected in the cities on the northern coastal plain of Shikoku Island where the wind is still calm. On the other hand, on the windward side of the Shikoku Mountains, the southern coastal plain of Shikoku Island is calm due to the blocking effect of the Shikoku Mountains. The location of the hydraulic jump is affected by the difference of the mountaintop height of the Shikoku Mountains. When the low-level southerly synoptic wind increases, the jump easily moves northward in lee of the col of the Shikoku Mountains, and the Yamaji-kaze begins first around Kawanoe.

Figure 20b displays a schematic picture of the Yamaji-kaze in its mature stage. The strong wind area near Kawanoe extends northward with the increase of the synoptic wind and forms a jet-like strong-wind area, spreading the break of the Yamaji-kaze front. This break of the Yamaji-kaze front propagates westward with the increase of the synoptic wind, and the onset of the Yamaji-kaze begins at Mishima and Doi successively from east to west. The surface wind is usually stronger at Doi than at Kawanoe. In the western part of the Shikoku Mountains, the Yamaji-kaze front shifts northward from the northern slope to the coastal plain, but it hardly moves up to Hiuchi-nada. In the western part of the coastal plain around Niihama, the surface wind is highly variable, reflecting the slight movement of the Yamaji-kaze front and a northerly wind is often observed. In the area before the hydraulic jump, the surface temperature is increased by the foehn. A northerly wind, opposite to the southerly downslope wind, prevails over the western part of Hiuchi-nada and the southern coastal

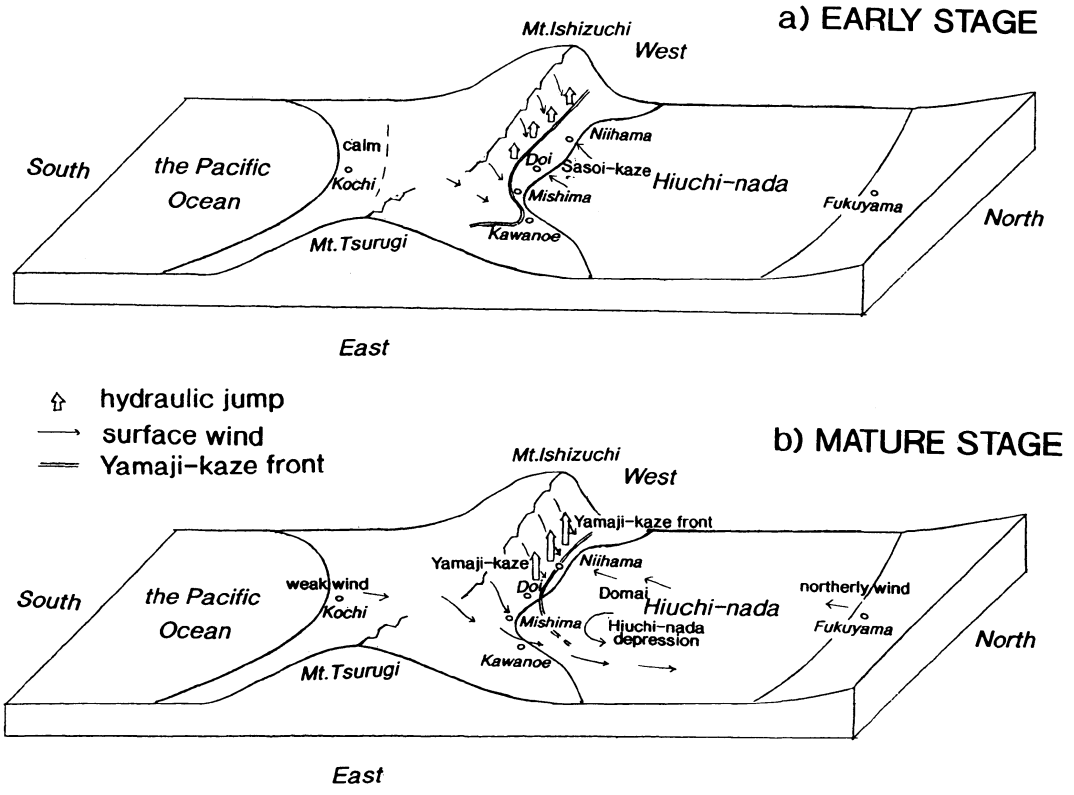


Fig. 20. Schematic representation of the conceptual model of the Yamaji-kaze. a) Early stage. b) Mature stage.

plain of the Chugoku Peninsula. This opposite wind corresponds to *Domai*. A cyclonic circulation corresponding to *Hiuchi-nada depression* develops between this northerly wind and the southerly jet-like strong-wind area in the lee of the col of the Shikoku Mountains. On the upstream side of the Shikoku Mountains, the southerly wind is usually weak due to the blocking effect of the Shikoku Mountains.

6. Summary and concluding remarks

Following the previous work (Saito and Ikawa, 1991a), the three dimensional effect of the orography of the Shikoku Mountains to the Yamaji-kaze was studied numerically, focusing on the effect of a col on the flow over a mountain range. Considering the fact that the Shikoku Mountains' height decreases in the central eastern part, a three-dimensional flow over a mountain range with a col is studied by a linear analytic solution and numerical experiments. Two parameters, lh_m, a non-dimensional mountain height and h_c/h_m, the ratio of the amplitude of the col to the mean ridge height, are used to prescribe the mountain shape in a homogeneous environmental atmosphere.

In the linear theory, the flow over a mountain range with a col in a homogeneous environmental atmosphere can be classified by lh_m and h_c/h_m into four régimes: a flow without wave breaking, a flow with wave breaking, a flow with wave breaking and flow splitting, and a flow with wave breaking and total blocking. The wave breaking occurs at $lh_m = 1$ for a mountain range without a col, while the critical value of lh_m above which wave breaking occurs decreases with the increase of h_c/h_m because the mountain wave is enhanced in the lee of the peak of the mountain range. The flow splitting occurs more readily with the increase of h_c/h_m. The total blocking occurs when lh_m is larger than 2 for a mountain range without a col, while the critical value of lh_m above which total blocking occurs increases with the increase of h_c/h_m.

In the numerical experiments, a three-dimensional non-hydrostatic model which employs an open inflow and outflow lateral boundary condition and a free-slip side lateral boundary condition is used. In the linear case, the numerical solution well agrees with the analytic solution. In the non-linear case, the wave breaking easily occurs in the lee of the peak of the mountain range and an internal hydraulic jump develops, while in the lee of the col, the wave breaking and the hydraulic jump hardly occur. The internal hydraulic jump which occurs in the lee of the peak of the mountain range tends to stay, while in the lee of the col the jump does not appear or it moves leeward rapidly. The behavior of the hydraulic jump is quite sensitive to the ex-

istence of the col, while the upstream blocking is rather insensitive to the existence of the col.

The flow régimes obtained by the the numerical experiments basically agree with those by the analytic solution, while critical values of lh_m which divide the flow régimes are about 20 % smaller than those predicted by the linear theory. The surface pressure drag normalized by the value in the linear theory conspicuously increases with the occurrence of the wave breaking, but when the upstream blocking occurs it no longer increases. When lh_m is small, the normalized pressure drag increases with the existence of the col, while when lh_m is large enough for flow splitting to occur, the pressure drag decreases with the existence of the col. The decrease of the effective height of the mountain due to upstream blocking might explain these experimental results. The maximum surface wind also conspicuously increases with the occurrence of wave breaking, while its increase is suppressed when upstream blocking or flow splitting occurs. For the two-dimensional mountain, the minimum surface wind occurs on the windward slope by upstream blocking, as the linear theory predicts, while for the mountain range with a col, it occurs in the lee of the mountaintop as the reversed flow behind a hydraulic jump when flow splitting occurs.

The response of the atmospheric hydraulic jump to the existence of a col is qualitatively analogous to the response of the hydraulic jump in shallow water flow to the magnitude of the channel width, which has been given by Saito (1992).

In order to simulate the Yamaji-kaze on 21 April 1987, numerical experiments are performed using the real orography of Shikoku Island under the observed thermal stratification and time-changing wind profile. The stay and shift of the hydraulic jump on the northern slope of the Shikoku Mountains, which correspond to the Yamaji-kaze front, and the extension of the strong surface wind area in the lee of the col of the Shikoku Mountains are successfully simulated. In the three-dimensional simulation, the occurrence of the reversed flow over Hiuchi-nada, which corresponds to *Domai*, is clearer when compared to the two-dimensional simulation. The movement of the Yamaji-kaze front is delayed and it tends to stay on the northern coastal plain of Shikoku Island in the three-dimensional simulation. One of the causes of the time lag between the onset of the simulated Yamaji-kaze and the observed one, which was too early in the two-dimensional simulation in Part 1, is attributed to the neglect of the three-dimensional effect of the orography. A further improved surface wind pattern is obtained by the inclusion of the surface friction through the restriction of the extent of the strong-wind area. The difference of the roughness between sea and land may affect the concentration of the downslope wind. An improved version of the conceptual model of the Yamaji-kaze is proposed on the basis of the results of the experiments.

As mentioned in Part 1, the development of the internal hydraulic jump and the reversed flow behind it depend on the formulation of the turbulent closure model, since they are associated with the wave breaking and are inherently non-linear phenomena. If we use Eq. (11) for the formulation of the mixing length even in the experiment without surface friction, the occurrence of a reversed wind behind the hydraulic jump becomes difficult for the two-dimensional isolated mountain. The horizontal resolution in the y-direction (5 km) used in our numerical experiments may not necessarily be sufficient to simulate the three-dimensional wave breaking. The phenomena dealt with in this study are highly non-linear ones, where the quantitative results in Section 4.2 might be influenced by the specification of the numerical model such as the computational scheme for the advection term, grid structures, and so on. A supplementary experiment using other models is a future subject.

The discussion in Section 4.3 seems to contain some important and unsolved problems. In Part 1, the similarities between the response of the internal hydraulic jump to the magnitude of the environmental wind speed and the behavior of the hydraulic jump in shallow water were presented. In this study, the similarity between the response of the internal hydraulic jump to the existence of a col and the response of the hydraulic jump in shallow water flow to the magnitude of the channel width are presented. This adds a new similarity to those between the hydraulic jump in a stratified atmosphere and the hydraulic jump in a shallow water. However, the similarities are qualitative ones. Recent studies (for example, Durran ,1986; Durran and Klemp, 1987; Smith, 1987; Smith and Sun, 1987) have attempted to make a correspondence between the behavior of a non-linear continuously stratified flow over a mountain and the hydraulic theory by introducing the concept of an *internal hydraulic theory*, but it seems that their attempts have not necessarily succeeded in every way. More studies should be conducted in order to understand further the analogy between the two.

The results of the simulations in Section 5.1 demonstrate that the experimental results in Section 4.2, which are performed under simple conditions, is applicable to a real situation. The basic features of the non-linear three-dimensional mountain flow presented in this study might be applied not only to the Yamaji-kaze but also to other downslope winds which occur in the lee of a mountain range with a col. However, the deformation of the behavior of the non-linear mountain flow by the factors of real situations such as asymmetry of the orography

or the existence of inversion layer are not thoroughly examined in this study. The vertical veering of the environmental wind and the temperature difference between the sea and the ground, which are neglected in simulations in Section 5.1, will also affect the wave breaking and the location of the Yamaji-kaze front. The effect of the Coriolis force did not notably affect the Yamaji-kaze itself in the experiment by Saito and Ikawa (1991b), but it deformed the flow pattern around Shikoku Island through the imbalance of the westward pressure gradient force in the upstream blocking region.

Although it is not realized in the simulation with surface friction in Section 5.1, when the synoptic wind is exceptionally strong the lee hydraulic jump may not occur due to the low non-linearity. In such a case, the Yamaji-kaze front no longer appears and southerly winds will prevail over the entire area from the northern coastal plain of Shikoku Island to the southern coastal plain of the Chugoku Peninsula, including Hiuchi-nada. It is reported that *Domai* is not observed when the synoptic southerly wind is very strong through the approach of a typhoon (Kobayashi, 1954). Although such a case may not be *typical* Yamaji-kaze and the ratio of the maximum surface wind to the environmental wind may decrease as suggested by Fig. 13 in Section 4.2, the magnitude of the maximum surface wind itself will still increase by virtue of the strong environmental wind.

The simulation presented in this study generally reproduces well the characteristics of the Yamaji-kaze, although the lateral boundary condition is still artificial and the initial condition is also simplified. To make a more realistic simulation of the Yamaji-kaze, a non-hydrostatic model which has adequate horizontal resolution (Δx, $\Delta y < 3$ km) will be required. An improvement of the model using an one-way nesting technique is under way (Saito and Ikawa, 1992). The results of the simulation of the Yamaji-kaze using the nested model will be reported at a later date.

Acknowledgements

The author expresses his heartfelt thanks to the late Dr. Motohki Ikawa of the Forecast Research Department of the MRI who gave valuable comments on this study. Thanks are extended to Drs. Kozo Ninomiya and Takehiko Furukawa of the JMA, and Professor Fujio Kimura of Tohoku University for their valuable comments. The author also wishes to express his thanks to Mr. Yoshihiro Takami of the Uwajima Meteorological Observatory for his courtesy for the permission to quote his figures. He is also obliged to Dr. Fumiaki Fujibe of the Forecast Research Department of the MRI for reading the manuscript and giving valuable comments. Numerical computations were conducted using MRI's computer systems, HITAC S810-10 and M280H.

References

Akiyama, To., 1956: On the occurrence of the local severe wind "Yamaji". Part 1. *J. Meteor. Res.*, **8**, 627–641 (in Japanese).

Arakawa, S., 1969: Climatological and dynamical studies on the local strong winds, mainly in Hokkaido, Japan. *Geophy. Mag.*, **34**, 349–425.

Arakawa, S. and F. Kimura, 1981: A numerical simulation of "Yamaji-kaze". *Draft of the annual meeting of the Japan Meteor. Soc.*, **40**, 113 (in Japanese).

Baines, P.G., 1987: Upstream blocking and air flow over mountains. *Ann. Rev. Fluid Mech.*, **19**, 75–97.

Bacmeister, J.T. and R.T. Pierrehumbert, 1988: On high-drag states of non-linear stratified flow over an obstacle. *J. Atmos. Sci.*, **45**, 63–80.

Clark, T.L., 1977: A small-scale dynamic model using terrain following coordinate transformation. *J. Comp. Phys.*, **24**, 186–215.

Crook, N.A., T.L. Clark and M.W. Moncrieff, 1990: The Denver cyclone. Part 1: Generation in low Froude number flow. *J. Atmos. Sci.*, **47**, 2725–2742.

Deardorff, J.W., 1980: Stratocumulus-capped mixed layers derived from a three-dimensional model. *Boundary-Layer Meteorol.*, **18**, 495–527.

Durran, D.R., 1986: Another look at downslope windstorms. Part 1: On the development of analogs to supercritical flow in an infinitely deep, continuously stratified fluid. *J. Atmos. Sci.*, **43**, 2527–2543.

Durran, D.R. and J.B. Klemp, 1987: Another look at downslope winds. Part 2: Nonlinear amplification between wave-overturning layers. *J. Atmos. Sci.*, **44**, 3402–13412.

Furukawa, T., 1966: On the "Yamaji Wind". *Tenki*, **13**, 261–268 (in Japanese).

Houghton, D.D. and A. Kasahara, 1968: Nonlinear shallow fluid over an isolated ridge. *Commun. Pure Appl. Math.*, **21**, 1–23.

Ikawa, M. and Y. Nagasawa, 1989: A numerical study of a dynamically induced foehn observed in the Abashiri-Ohmu area. *J. Meteor. Soc. Japan*, **67**, 429–458.

Ikawa, M., 1990: High drag states and foehns of a two-layered stratified fluid past a two-dimensional mountains. *J. Meteor. Soc. Japan*, **68**, 163–182.

Ikawa, M. and K. Saito, 1991: Description of a nonhydrostatic model developed at the Forecast Research Department of the MRI. *Tech. Rep. of the MRI*, **28**, 1–238.

Klemp, J.B. and R. Wilhelmson, 1978: The simulation of three-dimensional convective storm dynamics. *J. Atmos. Sci.*, **35**, 1070–1096.

Kobayashi, S., 1954: The mechanism and forecast of the local severe wind "Yamaji". *J. Meteor Res.*, **6**, 381–387 (in Japanese).

Kondo, J., 1975: Air-sea bulk transfer coefficients in diabatic conditions. *Boundary-Layer Meteor.*, **9**, 91–112.

Lilly, D.K. and J.B. Klemp, 1979: The effects of terrain shape on non-linear hydrostatic mountain waves. *J. Fluid Mech.*, **95**, 241–261.

Long, R.R., 1953: Some aspects of the flow of stratified fluids. 1. A theoretical investigation. *Tellus*, **5**, 42–58.

Long, R.R., 1954: Some aspects of the flow of stratified fluids. 2. Experiments with a two-fluid system. *Tellus*, **6**, 97–115.

Mellor, G., L. and T. Yamada, 1974: A hierarchy of turbulence closure models for planetary boundary layers. *J. Atmos. Sci.*, **31**, 1791–1806.

Miki, Y., 1988: The Yamaji-kaze (Case study). Technical Report submitted to the annual meeting of JMA for improvement of forecasting technique, Takamatsu Local Meteorological Observatory. 6–7 (in Japanese).

Miranda, P.M.A. and I.N. James, 1992: Non-linear three-dimensional effects on gravity-wave drag: Splitting flow and breaking waves. *Quart. J. Roy. Meteor. Soc.*, **118**, 1057–1081.

Orlanski, I., 1976: A simple boundary condition for unbounded hyperbolic flows. *J. Comp. Phys.*, **21**, 251–269.

Pierrehumbert, R.T. and B. Wyman, 1985: Upstream effects of mesoscale mountains. *J. Atmos. Sci.*, **42**, 997–1003.

Saito, K. and M. Ikawa, 1991a: A numerical study of the Local Downslope wind "Yamaji-kaze" in Japan. *J. Meteor. Soc. Japan*, **69**, 31–56.

Saito, K. and M. Ikawa, 1991b: The simulation of local winds by a three-dimensional nonhydrostatic model. Technical Report submitted to the annual meeting of JMA for improvement of forecasting technique, MRI, Forecast Research Department. 36–60 (in Japanese).

Saito, K., 1992: Shallow water flow having a lee hydraulic jump over a mountain range in a channel of variable width. *J. Meteor. Soc. Japan*, **70**, 775–782.

Saito, K. and M. Ikawa, 1992: Numerical simulation of local wind by a nonhydrostatic nested model. *Tenki*, **39**, 615–625 (in Japanese).

Smith, R.B., 1980: Linear theory of stratified hydrostatic flow past an isolated mountain. *Tellus*, **32**, 348–364.

Smith, R.B., 1985: On severe downslope winds. *J. Atmos. Sci.*, **42**, 2597–2603.

Smith, R.B., 1987: Aerial observations of the Yugoslavian Bora. *J. Atmos. Sci.*, **44**, 269–297.

Smith, R.B. and J. Sun, 1987: Generalized hydraulic solutions pertaining to severe downslope winds. *J. Atmos. Sci.*, **44**, 2934–2939.

Smith, R.B., 1989a: Mountain-induced stagnation points in hydrostatic flow. *Tellus*, **41**, 270–274.

Smith, R.B., 1989b: Comment on "Low Froude number flow past three-dimensional obstacles. Part 1: Baroclinically Generated lee vortices". *J. Atmos. Sci.*, **46**, 3611–3613.

Smith, R.B., 1991: Theory of 3-D mountain flow: Recent advances. Lecture at the 26th Colloquia on Oceanographic and Atmospheric Sciences in Tsukuba.

Smolarkiewicz, P.K. and R. Rotunno, 1989: Low Froude number flow past three-dimensional obstacles. Part 1: Baroclinically generated lee vortices. *J. Atmos. Sci.*, **46**, 1154–1164.

Smolarkiewicz, P.K. and R. Rotunno, 1990: Low Froude number flow past three-dimensional obstacles. Part 2: Upwind flow reversal zone. *J. Atmos. Sci.*, **47**, 1498–1511.

Sommeria, G., 1976: Three-dimensional simulation of turbulent processes in an undisturbed trade wind boundary layer. *J. Atmos. Sci.*, **33**, 216–241.

Takami, Y. and H. Ohnishi, 1988: On the "Yamaji-kaze". Proceeding Draft of the 1988 Annual Meeting of Osaka branch of Japan Meteor. Soc. 8–11 (in Japanese).

Takami, Y., 1990: Investigation of the "Yamaji-kaze" Part 4. Proceeding Draft of the 1990 Annual Meeting of Osaka branch of Japan Meteor. Soc. 376–377 (in Japanese).

やまじ風の数値的研究 (2)
—鞍部を伴う山脈を越える3次元の流れの非線形領域の振舞—

斉藤和雄
(気象研究所)

既報 (Saito and Ikawa, 1991a) に引き続く研究として、「やまじ風」に対する四国山地の地形の3次元的な効果が、山脈を越える流れに対する鞍部の影響に焦点を当てて数値的に調べられる。やまじ風の地理的な特徴が、鞍部を伴う山脈を越える3次元の流れの非線形領域の振舞によって説明される。

周期的な鞍部を伴う山脈を越える3次元の流れのレジームが、一様大気に対する線形解析解と非静水圧モデルを用いた数値実験によって調べられる。山の形状を記述するため、スコーラー数で無次元化した山の高さと、山の高さに対する鞍部の振幅の比の2つのパラメターが用いられる。数値解では、流れのレジームは線形論の予報する値に比べて20%程小さな山の高さから変化した。山脈が鞍部を伴う場合、山蔭後面では2次元モデルによる場合に比べて、より小さな山の高さから砕波が生じ、ハイドロリックジャンプの停滞と後面の逆風の発生が見られた。一方、鞍部の風下側では強風域は容易に風下側に拡大し、ジャンプ自体も不明瞭である場合が多い。ジャンプの振舞は、鞍部の存在による山脈の高さの違いに極めて敏感であるが、山脈風上側のブロッキングは、鞍部の有無に比較的鈍感である。鞍部の振幅の変化に対する内部ジャンプの振舞の応答は、浅水流に生ずるハイドロリックジャンプの流路幅の変化への応答 (Saito, 1992) と類似が見られる。

1987年4月21日の顕著なやまじ風を例に、観測された大気の鉛直プロファイルと中国山地の一部を含む四国の実地形を用いた数値実験が行われ、環境風が増大する場でのハイドロリックジャンプの振舞がシミュレートされる。2次元数値実験では早過ぎたやまじ風のオンセットのタイミングが、3次元数値実験では改善される事が示される。やまじ風の地理的な特徴が、四国山地山蔭でのジャンプの停滞とその後面の逆風、及び三島付近に抜ける鞍部風下側での強風域の拡がりによって説明される。地表摩擦の効果をシミュレーションに含める事によって、より現実的な地表風系が得られる。これらの3次元シミュレーションの結果を基に、やまじ風の概念モデルの改良版が示される。